The ultrastructural properties of the endoplasmic reticulum govern microdomain signaling in perisynaptic astrocytic processes

Audrey Denizot [1,2]*, María Fernanda Veloz Castillo [3,4,5], Pavel Puchenkov [6], Corrado Calì [4,5], Erik De Schutter [2]

1 AIstroSight, Inria, Hospices Civils de Lyon, Universite Claude Bernard Lyon 1, Villeurbanne, France
2 Okinawa Institute of Science and Technology, Computational Neuroscience Unit, Onna-Son, Japan
3 Biological and Environmental Science and Engineering Division, King Abdullah University of Science and Technology, Thuwal, Saudi Arabia
4 Department of Neuroscience, University of Torino, Italy
5 Neuroscience Institute Cavalieri Ottolenghi, Orbassano, Italy
6 Okinawa Institute of Science and Technology, Scientific Computing and Data Analysis section, Core Facilities, Onna-Son, Japan

* Corresponding author: audrey.denizot@inria.fr

Data availability statement: The data and code that support the findings of this study are openly available at https://zenodo.org/records/17106549 and https://github.com/adenizot/PAP-ER, respectively.

Acknowledgments: This work used the computing resources of the Scientific Computing and Data Analysis section from the Okinawa Institute of Science and Technology. We thank Iain Hepburn and Weiliang Chen (OIST, Japan) for discussion and advice on STEPS software. We thank Pierre Magistretti (KAUST, Thuwal) for the financial support of MFVC and of CC, and Graham Knott for kindly sharing the original EM dataset. This work was supported by a JSPS (Japan Society for the Promotion of Science) Standard Postdoctoral Fellowship for Research in Japan (21F21733).

Keywords: Neuroscience, glia, astrocyte, electron microscopy, tripartite synapse, calcium signaling, computational modeling

Main points

- 6 nm isotropic volume EM reveals that 75% of perisynaptic astrocytic processes (PAPs) contain some ER
- PAPs & ER of the same cell display diverse geometric properties
- Simulations in EM-derived meshes hint that ER geometry governs Ca^{2+} signals in PAPs

TOCI

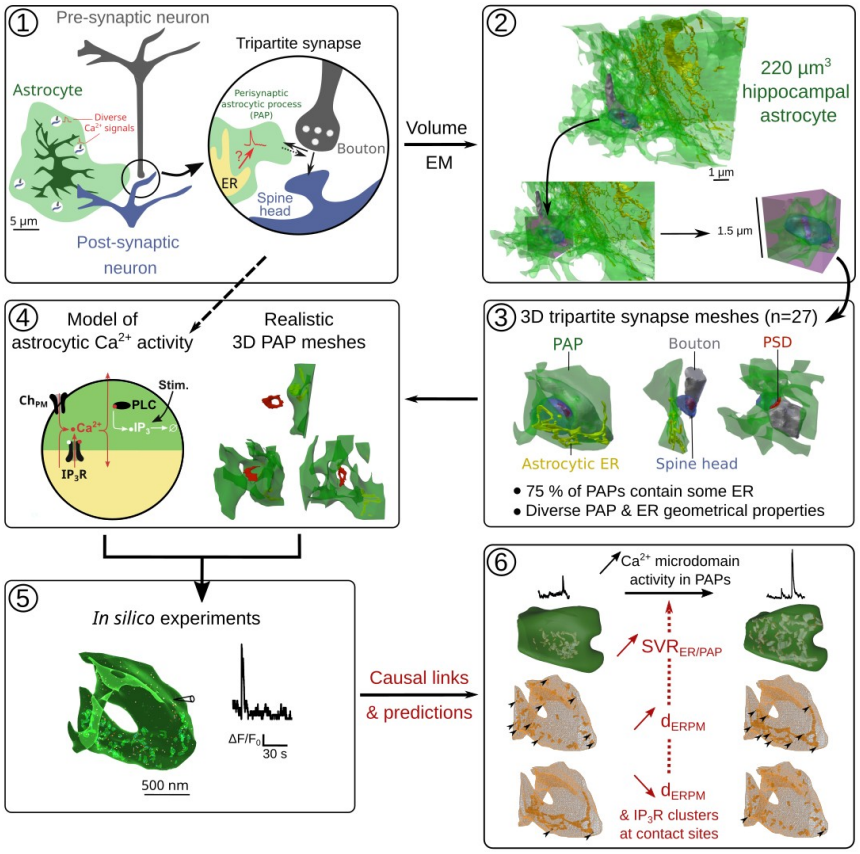

Abstract

Astrocytes are now widely accepted as key regulators of brain function and behavior. Calcium (Ca^{2+}) signals in perisynaptic astrocytic processes (PAPs) enable astrocytes to fine-tune neurotransmission at tripartite synapses. As most PAPs are below the diffraction limit, their content in Ca^{2+} stores and the contribution of the latter to astrocytic Ca^{2+} activity is unclear. Here, we reconstruct hippocampal tripartite synapses in 3D from a high resolution electron microscopy (EM) dataset and find that 75% of PAPs contain some endoplasmic reticulum (ER), a major calcium store in astrocytes. The ER in PAPs displays strikingly diverse shapes and intracellular spatial distributions. To investigate the causal relationship between each of these geometrical properties and the spatio-temporal

characteristics of Ca^{2+} signals, we implemented an algorithm that generates 3D PAP meshes by altering the distribution of the ER independently from ER and cell shape. Reaction-diffusion simulations in these meshes reveal that astrocyte activity is governed by a complex interplay between the location of Ca^{2+} channels, ER surface-volume ratio and spatial distribution. In particular, our results suggest that ER-PM contact sites can act as local signal amplifiers if equipped with IP_3R clusters but attenuate PAP Ca^{2+} activity in the absence of clustering. This study sheds new light on the ultrastructural basis of the diverse astrocytic Ca^{2+} microdomain signals and on the mechanisms that regulate neuron-astrocyte signal transmission at tripartite synapses.

Introduction

Astrocytes, the most abundant glial cells of the central nervous system, are essential for numerous brain functions and shape behavior [1, 2, 3]. In particular, astrocytes are key modulators of neurotransmission at tripartite synapses [4, 5]. A single astrocyte in the CA1 region of the mouse hippocampus is in contact with hundreds of thousands of synapses simultaneously, at perisynaptic astrocytic processes (PAPs) [6]. Around 75 % of cortical and 65 % of hippocampal synapses are contacted by an astrocytic process [7, 8]. This close contact between astrocytes and neurons allows astrocytes to control various synaptic functions, from glutamate uptake [9], and spillover [10, 11], to synapse homeostasis [12], stability [13], synaptogenesis [14], and neurotransmission [15, 5]. Those synaptic functions are associated with specific local molecular expression in PAPs [16, 17], which changes upon fear conditioning [16]. Importantly, the alteration of the proximity of PAPs

to hippocampal synapses of the CA1 region *in vivo* affects neuronal activity and cognitive performance [11]. Conversely, neuronal activity has been shown to induce the remodeling of synaptic coverage by PAPs in various brain regions, both *in vivo* and in acute slices [10, 18, 19, 13, 8, 20, 21, 22]. Together, these results illustrate that PAPs are preferential sites of neuron-astrocyte communication. Although the recent emergence of super-resolution techniques has provided key insights into the properties and functions of PAPs [23, 24], our understanding of PAP physiology and function in live tissue is hindered by their nanoscopic size [25, 26].

Ca^{2+} signals are commonly interpreted as a measure of astrocyte activity, notably in response to neurotransmitter release at synapses [27, 25, 28]. The recent advances in Ca^{2+} imaging approaches have improved the spatio-temporal resolution of Ca^{2+} signals monitored in astrocytes [29, 28]. Strikingly, it revealed that astrocytes in acute slices and *in vivo* exhibit spatially-restricted Ca^{2+} signals, also referred to as hotspots or microdomains, that are stable over time, and which activity varies under physiological conditions such as locomotion or sensory stimulation [30, 31, 32, 33, 34, 35, 36, 37, 38, 39, 40, 41, 42]. Growing evidence supports that PAPs are preferential sites displaying spatially-restricted Ca^{2+} microdomains in response to neurotransmission [40, 41, 43, 44, 30]. As a single astrocyte can contact hundreds of thousands of synapses simultaneously [6], such spatially-restricted Ca^{2+} microdomains might enable the astrocyte to finely tune synaptic transmission at the single synapse level.

mGluR activation on the astrocytic membrane following

neurotransmission at glutamatergic synapses results in Ca^{2+} transients mediated by G_q proteins and Ca^{2+} stores such as the endoplasmic reticulum (ER) [29], which can trigger the release of molecules that modulate neurotransmission, gliotransmitters [45, 46, 15, 5]. Most astrocytic Ca^{2+} signals are mediated by the Inositol 3-Phosphate (IP_3) receptors on the membrane of the endoplasmic reticulum (ER) [47]. Because of their nanoscopic size, the Ca^{2+} pathways involved in microdomain Ca^{2+} signals in PAPs are still unclear. In particular, the presence of ER in PAPs and its involvement in microdomain Ca^{2+} signals at synapses are highly debated. During the last decade, PAPs have been regarded as devoid of ER, with a minimum distance between the synapse and the closest astrocytic ER > 0.5 μm [48, 25, 49]. In contrast, recent studies suggest that Ca^{2+} activity in PAPs partly results from Ca^{2+} fluxes from the ER. Notably, inhibiting ER-mediated Ca^{2+} signaling in fine processes results in a decreased number of Ca^{2+} domains (Figure 4N-Q of [32]) and a decreased Ca^{2+} peak frequency [32, 44, 39]. Furthermore, some astrocytic ER has been detected near synapses in recent EM studies [26, 50]. Yet, the geometrical properties of the ER in PAPs and its distribution remain poorly characterized, but could have a strong impact on neuron-astrocyte communication at tripartite synapses.

Recent advances in electron microscopy (EM) enable the resolution of the ultrastructure of astrocytes at an unprecedented spatial resolution. Here, we reconstruct 46 three dimensional meshes of tripartite synapses from a 220 μm^3 hippocampal astrocytic volume from the CA1 stratum radiatum region (6 nm voxel resolution) [51], reconstructed from electron microscopy (EM). Strikingly, we find that 75 % of PAPs in this dataset contain some ER, which can be as close as 72 nm to the post-synaptic

density (PSD). Analysis of the geometrical features of these meshes reveal the vast diversity of ER shapes and distributions within PAPs from a single cell. We then used a detailed stochastic reaction-diffusion model of Ca^{2+} signals in PAPs to investigate the mechanistic link between the spatial characteristics of the ER measured in the 3D meshes and the spatio-temporal properties of Ca^{2+} microdomain activity in PAPs. To be able to decipher the effect of ER distribution within the PAP independently from the effect of its shape, we developed an algorithm that automatically creates realistic 3D tetrahedral PAP meshes with various ER distributions based on realistic meshes reconstructed from EM. *In silico* experiments in these meshes reveal that the spatio-temporal properties of Ca^{2+} signals in PAPs are tightly regulated by the intracellular geometry. Together, this study provides new insights into the geometrical properties of hippocampal tripartite synapses and predicts causal links between these features and Ca^{2+} microdomain activity at tripartite synapses.

2 Methods

2.1 3D reconstruction from electron microscopy

2.1.1 Sample preparation and imaging

The original dataset used in this work (EM stack and 3D reconstructions) was previously published in [51]. The block was a gift from Graham Knott (BioEM imaging facility at EPFL, Lausanne, Switzerland). All procedures were performed according to the Swiss Federal Laws.

One P90 Sprague-Dawley rat was deeply anesthetized with isoflurane and transcardially perfused using 2 % paraformaldehyde and 2.5 % glutaraldehyde in
PBS 0.1M. Coronal sections (100 μm) were obtained and washed in cacodylate buffer, followed by a post-fixation using osmium tetroxide and uranyl acetate. Finally, the sections were embedded in Durcupan. Regions of the hippocampus were dissected under a stereoscopic microscope, mounted onto a blank resin slab, and trimmed using an ultramicrotome (Laica Ultracut UC-7). Imaging was performed using an NVision 40 FIB-SEM (Carl Zeiss) with an acceleration voltage of 1.5 kV, a current of 350 pA, and a dwell time of 10 μs/pixel. Serial images were obtained using backscattered electrons and collected at a 6 nm/pixel magnification and a 5 nm milling depth between images.

2.1.2 3D reconstruction and rendering

The serial micrographs were first registered using Multistackreg, a freely

available plug-in for Fiji [51]. Then, using those micrographs, we proceeded to the image segmentation and 3D model reconstructions by using TrackEM2 (a plug-in for Fiji) for manual segmentation, and iLastik, for a semi-automated segmentation. The extracted models were then imported into Blender software for visualization and rendering purposes [52].

2.1.3 Extraction of tripartite synapse meshes

For each synapse in contact with the 220 μm^3 astrocytic volume, a cube of edge length 1.5 μm (3.375 μm^3) was created and centered at the center of mass of the PSD. All of the elements of the mesh (astrocyte, astrocytic ER, spine and bouton) that were within the cubic volume were isolated using a boolean intersection operator available in Blender, forming what we refer to as a tripartite synapse mesh.

The size of the cube was chosen to be large enough to contain the whole spine and bouton elements while containing a single synapse, taking into consideration that the neuropil is believed to contain around one synapse per micrometer cube. This workflow resulted in the creation of 44 excitatory and 2 inhibitory synapse meshes.

2.2 3D mesh manipulation

All 3D mesh manipulations were performed with open-access, open-source software. All 3D meshes used in this study are freely available under the Creative Commons Attribution 4.0 International license at https://zenodo.org/records/17106549.

2.2.1 3D PAP mesh processing for reaction-diffusion simulations

PAP meshes from tripartite synapse meshes were pre-processed using Blender software to be suitable for reaction-diffusion simulations. The workflow is illustrated in Fig. S8. Intersection between ER and PAP membranes was prevented by using a boolean intersection operator. ER was relocated a few nanometers away from the plasma membrane. PAP compartments that were disconnected from the largest PAP volume were deleted. Boolean difference operation was performed between the PAP and ER elements. Non-manifold vertices were repaired. The resulting PAP surface mesh was exported in stl format, which was then converted into a 3D tetrahedral mesh (msh format) using TetWild software [53]. Lastly, the mesh was imported into Gmsh software to be converted into 2.2 ASCII format, supported by the STEPS mesh importer.

2.2.2 Generation of realistic PAP meshes with various ER distributions and constant shape and size

We have implemented a script that generates realistic 3D tetrahedral PAP meshes characterized by various ER locations, constant ER shape and size. The algorithm is written in Python, can be imported in Blender, and is available at https://github.com/adenizot/PAP-ER. The workflow is presented in Fig. 5A. First, all elements of the mesh, i.e. the PAP and the ER, are relocated so that their center of mass are centered at the origin. Then, the ER is split into smaller ER objects using a custom-made function. Briefly, n cubes of a given size are placed along the ER object. Intersection boolean operation is then performed between the ER and each cube, resulting in the creation of n ER objects. ER objects smaller than 30 nm^3 are deleted. The remaining ER objects are rescaled so that

the sum of their surface areas matches the area of the original ER element, measured with the “3D Print” Blender add-on. The number and size of cubes can be altered depending on the size of the original ER and on the mesh characteristics desired. Using Blender’s physics engine, a simulation with m frames is generated, in which ER objects are subject to physical forces that alter their location between each frame. The input of the “RunPhysics” function includes parameters that affect how close objects can get, which can be altered to prevent membrane intersection. Note that parameter values used in the ER splitting and scattering functions should be adjusted depending on the mesh used (see the repository at https://github.com/adenizot/PAP-ER for more details). Examples of frames generated by this workflow applied to d1s15a32b1 PAP mesh are presented in Supplementary movie 3. For each selected frame, the mesh pre-processing steps presented in Fig. S8 are performed automatically, resulting in the export of a surface mesh (stl format). 3D meshing and format conversion can then be performed using TetWild and Gmsh software, as described above. The resulting meshes can be used to perform reaction-diffusion simulations.

2.2.3 Analysis of the geometrical properties of 3D meshes

The volume and surface area of each synaptic element, i.e. the PAP, astrocytic ER, spine head, and bouton, were measured using the Blender add-on “3D Print”. We implemented a Python script that can be imported in Blender 4.3.2. software (https://www.blender.org/) that measures distances between the mesh elements of interest. The code is available at https://github.com/adenizot/PAP-ER. The distance between each vertex of the plasma membrane (PM) of the PAP and the center of mass of the neighboring PSD, and the closest vertices on the bouton and spine

head membranes were computed in Blender and stored in a list. Similarly, ER-PSD distance was analyzed by measuring the distance between each vertex of the ER membrane and the center of mass of the PSD. To characterize the distribution of the ER, for each vertex on the PM, the closest ER vertex was detected and its distance to the PM vertex was stored in a list. To compare the distribution of the ER in different 3D meshes, we computed the median of ER-PM distances in each mesh: d_{ERPM}. PAP-PSD, PAP-Bouton, PAP-Spine, ER-PSD, and ER-PM distance lists were exported to a text file for analysis and visualization.

2.3 Computational modeling

2.3.1 Modeled reactions and computational approach

Astrocytic Ca^{2+} signals in PAPs were simulated using the reaction-diffusion voxel-based model of ER-dependent Ca^{2+} signaling from Denizot and colleagues ([54] Table 2, Fig. 6-7). The kinetic scheme is presented in Figure 3A and Table S2. Parameter values and initial conditions are detailed in Table S3. Briefly, the model describes Ca^{2+} fluxes in and out of the astrocytic cytosol. The opening of IP_3R channels on the ER membrane triggers Ca^{2+} influx in the cytosol. IP_3 can be synthesized by the Ca^{2+}-dependent activity of Phospholipase C (PLC) δ. IP_3 removal from the cytosol is described by a decay rate. IP_3R dynamics is derived from the De Young & Keizer's model [55]. Each IP_3R has 3 binding sites: one to IP_3 and two to Ca^{2+} (activating and inhibiting). The channel can thus be in 8 different states. The open state is {110}: IP_3 and Ca^{2+} are bound to the activating sites and the Ca^{2+} inactivating site is unbound. Endogenous Ca^{2+} buffers are not explicitly modeled and their effect on Ca^{2+} dynamics is accounted for by decreasing the effective Ca^{2+} diffusion coefficient, as

previously described [54, 56]. In a subset of simulations, GCaMPs6s, genetically-encoded Ca^{2+} indicators [29], were added to the cytosol and variations of [Ca-GCaMP] concentration, mimicking experimental Ca^{2+} imaging, were measured. For further details on the model assumptions, please refer to the original paper presenting the model [54]. We slightly altered this model to better describe and control IP_3R-independent Ca^{2+} fluxes. To do so, IP_3R-independent Ca^{2+} influx was modeled as an influx through Ca^{2+} channels at the plasma membrane, Ch_{PM}. For simplicity, the number of Ch_{PM} channels was the same the total number of IP_3R channels, N_{IP3R}. Ca^{2+} influx rate at Ch_{PM} channels, γ, is $3 \times 10^{-2}\ s^{-1}$.

The model was implemented using the STochastic Engine for Pathway Simulation (STEPS) (http://steps.sourceforge.net/) 3.5.0 [57, 58]. This software uses a spatialized version of Gillespie's SSA algorithm [59] to perform exact stochastic simulations of reaction-diffusion systems. Simulations in STEPS allow the diffusion of molecules in 3D tetrahedral meshes and onto the surfaces of the mesh, such as the ER and plasma membrane. STEPS allows volume and surface reactions. Reactions can occur only between molecules within the same tetrahedron (volume reactions) or in adjacent triangle and tetrahedron (surface reactions). Boundary conditions were reflective. The simulation time was 100 s. The states and amounts of all molecular species were measured at each time step (1 ms).

2.3.2 Neuronal stimulation simulation

Unless specified otherwise, glutamatergic transmission at the synapse was modeled and occurred at simulation time t=1 s. To do so, IP_3 molecules were injected in tetrahedra below the plasma membrane of the

PAP, emulating IP_3 synthesis resulting from the activation of metabotropic glutamatergic receptors at the membrane of the PAP. Supplementary movie 4 presents a visualization of a simulation at neuronal stimulation time, in the d2s6a9b1 PAP mesh.

2.3.3 Simulation code

Simulations were performed using the model of Ca^{2+} signals in fine processes from Denizot and collaborators [54], available at https://github.com/ModelDBRepository/247694.

The simulation code used in this study is available at https://github.com/adenizot/PAP-ER.

2.3.4 Ca^{2+} residency time analysis

Ca^{2+} residency time was measured by performing n=16 simulations for each value of median d_{ERPM}. In each simulation, for each IP_3R, we injected a single Ca^{2+} ion in the IP_3R site nanodomain. These regions of interest contained 15-16 tetrahedra each, consisting of the tetrahedron in contact with the IP_3R triangle, neighboring tetrahedra, and tetrahedra in contact with the latter. Then, we tracked the time it took for the Ca^{2+} ion to diffuse away from the nanodomain.

2.3.5 Ca^{2+} peak detection and characterization

Ca^{2+} peaks were considered initiated and terminated when Ca^{2+} concentration increased above and decreased below peak threshold, respectively. Peak threshold was $[Ca]_b + n\sigma_{Ca}$, where $[Ca]_b$ is the basal Ca^{2+} concentration and σ_{Ca} is the standard deviation of the $[Ca^{2+}]$

histogram in the absence of neuronal stimulation. n varied depending on the signal/noise ratio of the simulation of interest, notably when measuring Ca-GCaMP signals, noisier than free Ca^{2+} signals (see *e.g.* Fig 3C). Ca^{2+} peak frequency, duration, and amplitude were measured in each simulation. Ca^{2+} peak duration corresponds to the time between peak initiation and termination. Ca^{2+} peak amplitude corresponds to the maximum number of Ca^{2+} ions measured during peak duration. Peak amplitude is expressed as the number of Ca^{2+} ions (# Ca) in the cytosol of the whole PAP. Ca^{2+} peak frequency corresponds to the amount of peaks detected during the simulated time. The number of IP_3R peak opening events was recorded at each time step, in the whole PAP.

2.4 Statistical analysis

Data analysis and statistics were performed using open-access and open-source software: the SciPy and Pandas Python libraries. Data visualization was performed using Seaborn and Matplotlib Python libraries. The sample size for each analysis, n, is described in the figure legend. Before statistical analysis, the normality of the data distribution was inferred using the Shapiro-Wilk test. The relationship between Ca^{2+} peak characteristics and parameter values was inferred using one-way ANOVA if values followed a Gaussian distribution, Kruskal-Wallis one-way ANOVA otherwise. The linear relationship between two datasets was evaluated using Spearman's correlation coefficient. The test and p-value, p, associated with each analysis is described in the legend of the associated figure or in the main text.

3 Results

3.1 Quantification of the geometrical properties of hippocampal tripartite synapses

To characterize the geometrical properties of tripartite synapses, we used a 220 μm^3 (7.07 μm x 6.75 μm x 4.75 μm) hippocampal astrocytic volume from the CA1 stratum radiatum region reconstructed from a perfectly isotropic EM stack (6 nm voxel resolution) [51]. Elements from the neuropil, i.e. boutons, dendritic spine heads, and post-synaptic densities (PSDs), were also reconstructed. Following the workflow presented in Fig. 1A, forty-four excitatory and two inhibitory tripartite synapse meshes were reconstructed, containing all elements belonging to the astrocyte and to the neuropil within a cube of 1.5 μm edge length (3.375 μm^3) centered at the center of mass of the PSD (Supplementary Movie 1). Five of those tripartite synapse meshes are displayed in Fig. S1. Among these meshes, seventeen were located at the borders of the 220 μm^3 astrocytic volume and thus could not be fully reconstructed. They were thus excluded from the quantitative analysis. The surface area, volume, and surface-volume ratio (SVR) of each synaptic element, i.e. the PAP, astrocytic ER, spine, and bouton, of the remaining twenty-seven fully reconstructed excitatory tripartite synapses are presented in Fig. 1C, D, F, respectively, and in Supplementary Table S1. Interestingly, we found a strong positive correlation between spine head and bouton volume (Fig. 1E), hallmark of synapse stability [60]. The large PAP SVR and smaller spine head and bouton SVRs reported here are in line with previous reports (see e.g. [49, 61] and Fig. S2). The distance between each vertex on the PAP membrane and the center of mass of the PSD was measured

in each of the 27 meshes (Fig. 1B), providing a quantification of the distribution of the astrocyte around the synapse. Our results highlight the diverse distances between PSDs and PAPs belonging to a single cell. In line with previous studies [8, 62, 48], PAP membrane vertices could be as close as 5 nm to the PSD, with an average distance between the PSD and the closest PAP vertex of 65 nm. Importantly, PAPs were closer to the PSD than boutons and spines (Fig. 1G). The distance between PAPs and neuropil structures did not vary depending on the presence of ER in the PAP. Importantly, PAPs were closer to larger boutons and larger spines (Fig. 1H). Supplementary figures S3 and S4 display the distributions of the distances between each vertex of the membranes of PAPs and the closest spine (Fig. S3) or bouton (Fig. S4) vertex. Finally, we found that small PAP-PSD distances were correlated with large PAP surface area (Fig. 2H) and small bouton and spine surface areas (Fig. S5). Note that PAPs that were closer to boutons were also closer to spines and that bouton and spine size were positively correlated, while no correlation was found between PAP size and bouton or spine head size (Fig. S5). Overall, we report a high variability of the geometrical properties of PAPs belonging to the same astrocyte, which are correlated to the size of the neighboring synaptic elements.

3.2 Geometrical properties of the endoplasmic reticulum in perisynaptic astrocytic processes

Because of the nanoscopic size of most PAPs, the Ca^{2+} pathways that regulate astrocytic Ca^{2+} microdomain activity at tripartite synapses remain to be uncovered. Notably, the presence of ER in PAPs is controversial

[48, 26, 50, 63]. We have thus investigated the presence and geometrical properties of the ER in the PAPs from the 27 fully reconstructed excitatory tripartite synapse meshes presented in Fig. 1.

75 % of PAPs contained some ER (Fig.2A-D), which challenges previous observations that reported that tripartite synapses are devoid of astrocytic ER. ER surface area, volume, and SVR were highly variable between PAPs of the same cell (Fig. 2C). Importantly, bouton, spine, and PAP surface area, volume, and SVR did not differ depending on the presence of ER in the PAP (Supplementary Fig. S6). In addition, we characterized the vicinity of the astrocytic ER to the synapse. To do so, we measured the distance between each vertex on the ER membrane to the center of mass of the PSD (n=20). We found that ER-PSD distance varies drastically from synapse to synapse (Fig. 2F-G) and can be as little as 70 nm, far below the > 0.5 μm ER-PSD distance reported previously [48, 25]. The closest ER vertex was on average 432 nm away from the center of mass of the PSD. Interestingly, the larger the surface area of the ER, the closer it was to the PSD (Fig. 2G). Astrocytic ER was closer to the PSD in PAPs with higher surface area (Fig. 3G). ER surface area and ER-PSD distance were not correlated to the surface area of the PAP, spine, or bouton (Fig. S7A-B).

We next aimed at quantifying ER-PM distance, d_{ERPM}. To do so, we measured the distance between each vertex on the plasma membrane (PM) and the closest vertex on the ER. We found that d_{ERPM} is highly variable in PAPs from a single cell, with a median d_{ERPM} from around 200 nm to 1200 nm (Fig. 2H). Not surprisingly, median d_{ERPM} was negatively correlated with ER and PAP surface area (Fig. S7C). Interestingly, d_{ERPM} was negatively correlated to bouton surface area (Fig. 2H, $p = 0.01$).

Importantly, we found that PAPs closer to the synapse were characterized by a lower median ER-PM distance (Fig. 2H, $p = 1.14 \times 10^{-4}$). Note that there was no correlation between d_{ERPM} and spine surface area (Fig. S7C).

Overall, our results highlight that, in the hippocampal CA1 stratum radiatum astrocyte volume reconstructed in this study, most astrocytic nanoscopic compartments that interact with synapses, PAPs, contained some ER. ER shape was highly variable, and was distributed closer to the plasma membrane in PAPs that were closer to the synapse. These correlational observations could have strong implications on ER-dependent Ca^{2+} signaling in PAPs resulting from synaptic transmission.

3.3 Reaction-diffusion simulations reveal different spatiotemporal properties of Ca^{2+} signals in PAPs of the same cell

PAPs are characterized by highly diverse sizes and distributions of the ER (Fig. 2), which could affect ER-mediated Ca^{2+} signals in PAPs. Because of their nanoscopic size, measuring Ca^{2+} activity and deciphering the involvement of ER-mediated signals in individual PAPs in live tissue is extremely challenging [28]. The mechanistic link between the geometrical properties of the ER and the spatiotemporal properties of Ca^{2+} microdomain signals in PAPs is thus unclear and hard to test experimentally. Yet, understanding the mechanisms that govern PAP activity is critical to deepen our understanding of neuron-astrocyte communication. Here, we use the PAP meshes extracted from EM presented in Fig. 2 together with a spatial stochastic model of Ca^{2+}

signaling adapted from the model of Denizot and collaborators [54] to investigate the mechanistic link between ER shape and Ca^{2+} microdomain activity in PAPs. Ca^{2+} influx in the PAP cytosol in the model is mediated by Inositol 3-Phosphate (IP_3) receptors on the membrane of the ER and by Ca^{2+} channels at the plasma membrane, Ch_{PM}. The reactions modeled are presented in Fig. 3A, Supplementary Tables S2, S3, and in the Methods section. Neuronal activity was simulated at t=1 s by infusing 50 IP_3 molecules at the PM of the PAP. The implementation of this model with STEPS software [64] allows simulations to be carried out in tetrahedral meshes in three spatial dimensions, such as the ones reconstructed in this study. Representative Ca-GCaMP traces, corresponding to the concentration of Ca^{2+} bound to Ca^{2+} indicators added to the cytosol of the model, display spatio-temporal characteristics similar to Ca^{2+} signals measured in organotypic hippocampal astrocytic cultures [65] (Fig. 3B).

We performed simulations in six PAP meshes reconstructed from electron microscopy, characterized by various geometrical properties of the ER: d1s3a107b1, d1s8a22b1, d1s10a24b1, d2s6a9b1, d9s4a34b1 and d10s1a2b1 (Fig. 3C, Table 1). To do so, meshes were pre-processed to allow their use in reaction-diffusion simulations. The pre-processing workflow is described in Fig. S8 and in the Methods section. Ca-GCaMP and free Ca^{2+} signals, in simulations with and without Ca^{2+} indicators in the cytosol, respectively, were measured in d1s3a107b1, d1s8a22b1, d1s10a24b1, d2s6a9b1, d9s4a34b1 and d10s1a2b1 PAP meshes. A simulation in PAP d9s4a34b1 is shown in Supplementary movie 2. Representative traces are displayed in Fig. 3C. Peak frequency (Fig. 3D), duration, and amplitude (Fig. S9) varied greatly depending on the mesh.

In accordance with previous studies [54, 66], Ca-GCaMP and free Ca^{2+} signals displayed different spatio-temporal properties (Fig. 3D and S9). These results suggest that the diverse geometrical features of PAPs and ER reported in Fig. 1 and 2, respectively, are correlated with different Ca^{2+} microdomain spatio-temporal properties. d1s3a107b1, d1s8a22b1, d1s10a24b1, d2s6a9b1, d9s4a34b1 and d10s1a2b1 PAPs displayed different ratios between the ER surface area and the cytosolic volume, $SVR_{ER/PAP;}$, and median ER-PM distance d_{ERPM}. Interestingly, Ca^{2+} peak frequency, IP_3R opening frequency (Fig. 3 E-F), and Ca^{2+} peak amplitude and duration (Fig. S9C-D) were positively correlated with $SVR_{ER/PAP}$ and negatively correlated with d_{ERPM}. As the computational model explicitly describes the cytosolic compartment and the ER surface area but ignores intra-ER dynamics, we focused this study on the geometrical properties that alter ER surface properties. Consequently, geometrical features such as the ER volume or the fraction of PAP volume occupied by the ER, although positively correlated to Ca^{2+} peak activity (Fig. S10), were not considered in this study.

3.4 Ca^{2+} microdomain activity in PAPs increases with ER surface-PAP volume ratio

As Ca^{2+} peak frequency and IP_3R opening frequency were positively correlated with the ratio between the ER surface area and the PAP volume, $SVR_{ER/PAP}$ (Figure 3E), we next aimed at inferring the causal relationship between $SVR_{ER/PAP}$ and Ca^{2+} microdomain activity. To do so, we created meshes with various ER surface area, while maintaining ER and PAP shapes. The original mesh was extracted from the 220 μm^3

astrocytic volume, located at the vicinity of the d9s3a51b1 PSD and referred to as PAP1 (Fig. S11). Meshes with various $SVR_{ER/PAP}$ were created from PAP1 by rescaling the ER using Blender software. Tetrahedral PAP meshes were then created following the mesh pre-processing workflow described in Fig. S8, resulting in the creation of $PAP1_v$, $PAP1_w$, $PAP1_x$, $PAP1_y$ and $PAP1_z$ meshes (Fig. 4A). The geometrical properties of those meshes are presented in Table 1.

Spontaneous IP_3R opening frequency (Fig. 4B), Ca^{2+} peak frequency (Fig. 4C), duration (Fig. S12A), and amplitude (Fig. S12B) increased with $SVR_{ER/PAP}$. Interestingly, neuronal stimulation resulted in an increase of IP_3R opening frequency (Fig. 4B) and was encoded in peak frequency (Fig. 4C) but did not significantly alter peak amplitude and duration (Fig. S12A-B). The increased IP_3R opening and peak frequency with $SVR_{ER/PAP}$ are not surprising as ER surface area S_{ER} increases with $SVR_{ER/PAP}$ in those meshes. As IP_3R density was constant across simulations, increasing S_{ER} thus resulted in an increase of the amount of IP_3R channels with $SVR_{ER/PAP}$. The total number of IP_3R channels, N_{IP3R}, thus was 24, 120, 240, 360 and 460, in $PAP1_v$, $PAP1_w$, $PAP1_x$, $PAP1_y$ and $PAP1_z$ meshes, respectively. However, simulations with the same number of IP_3R channels as $PAP1_z$, 460, were performed in $PAP1_w$, $PAP1_x$, $PAP1_y$, and $PAP1_z$ meshes (Supplementary Fig. S13) and confirmed that $SVR_{ER/PAP}$ influences IP_3R opening frequency and thus Ca^{2+} peak frequency. Simulations in these meshes replicated the correlation

between $SVR_{ER/PAP}$ and Ca^{2+} peak frequency and IP_3R opening frequency observed in Fig. 3. No correlation was found between $SVR_{ER/PAP}$ and peak amplitude or duration (Fig. S13C-D). Note that no Ca^{2+} signals were detected in $PAP1_v$ mesh.

Importantly, we noticed that increasing $SVR_{ER/PAP}$ in PAP1 resulted in a decrease of the median distance between the ER and the plasma membrane (PM) in the PAP, d_{ERPM} (Fig. 4D), so that IP_3R opening frequency and Ca^{2+} peak frequency were positively correlated with d_{ERPM} (Fig. 4E-F). Moreover, d_{ERPM} was also positively correlated with IP_3R opening and Ca^{2+} peak frequency in meshes from Fig. 3. To differentiate the effect of d_{ERPM} from the effect of $SVR_{ER/PAP}$ on Ca^{2+} dynamics, we next developed an algorithm to alter ER-plasma membrane distance independently of the shape, surface area, and volume of the ER and PAP.

3.5 Ca^{2+} microdomain activity is altered by the spatial distribution of the ER

To discern the effect of $SVR_{ER/PAP}$ from the effect of d_{ERPM} on Ca^{2+} microdomain activity in PAPs reported in Fig. 3 and 4, we implemented an algorithm that generates realistic tetrahedral 3D meshes of PAPs characterized by various distributions of the ER within the same PAP with constant $SVR_{ER/PAP}$. The workflow is presented in Fig. 5A. Briefly, the ER is split into small portions, then resized to match the total ER surface area of the original mesh. A simulation of n frames is then generated in Blender, which alters the location of the ER objects within the PAP. Each frame is thus characterized by a unique distribution of the ER objects within the PAP, while ER and PAP shape, surface area, volume, and SVR

are constant across frames (Supplementary movie 3). The mesh processing workflow presented in Fig. S8 is then automatically applied to each frame of interest. This workflow allows the creation of numerous 3D PAP meshes characterized by various d_{ERPM}, that can be used for reaction-diffusion simulations in 3D. The workflow successfully produced realistic tetrahedral PAP meshes characterized by various d_{ERPM}, where d_{ERPM} decreased and the surface area of the ER at contact sites increased with frame number (Fig. 5B, workflow applied to PAP d1s15a32b1). The Blender file, python script, and parameter values used to generate these meshes are available at https://github.com/adenizot/PAP-ER.

Representative Ca^{2+} traces in meshes with various median d_{ERPM} are presented in Fig. 5C. IP_3R channels were located at ER-PM contact sites, *i.e.* on the triangles of the ER surface that were the closest to a plasma membrane triangle. First, we checked that splitting the ER did not significantly alter Ca^{2+} activity in PAP meshes (Supplementary Fig. S14), which is possible because intra-ER Ca^{2+} dynamics is not considered in the model. Simulations in these meshes suggest that increasing median d_{ERPM} can trigger an increase in IP_3R opening frequency and Ca^{2+} peak frequency, when IP_3Rs are located at ER-PM contact sites (Fig. 5D). This increase is associated with an increase in the proportion of IP_3Rs that get active at least once during simulation time (Fig. 5D). Note that Ca^{2+} peak amplitude and duration slightly increased with median d_{ERPM} (Fig. 5F). These results were confirmed by simulations in another realistic PAP mesh (Fig. S15). Interestingly, this suggests an opposite effect of d_{ERPM} on Ca^{2+} peak properties to that observed in Fig. 3F. This indicates that $SVR_{ER/PAP}$ was probably the main determining factor of the variability of simulated Ca^{2+} peak frequency in the PAP meshes extracted from EM

presented in Fig. 3. The observed correlation between d_{ERPM} and Ca^{2+} peak frequency most probably reflected an indirect effect of $SVR_{ER/PAP}$, as $SVR_{ER/PAP}$ and d_{ERPM} were negatively correlated (Spearman correlation coefficient r=-0.81, p = 8.45×10^{-11}).

The simulation results presented in Fig. 5 suggest that a distribution of the ER further away from the plasma membrane can amplify peak frequency in the absence of IP_3R clustering. This may seem counter-intuitive as ER-PM contact sites are often described as hubs of signal amplification. We hypothesize that, in the absence of IP_3R clusters, increasing d_{ERPM} increases the probability of Ca^{2+} ions to diffuse away from contact sites, and thus increases the probability that it can reach a new IP_3R channel to activate. To test this hypothesis, we measured the minimum distance between each pair of neighboring IP_3Rs, d_{IP3R}. We found that d_{IP3R} decreased and was less variable as median d_{ERPM} increased, confirming our intuition (Fig. 5E). We also confirmed that d_{ERPM} at IP_3R sites increased with median d_{ERPM} (Fig. S16A), which could allow a faster diffusion of Ca^{2+} away from ER-PM contact sites to activate nearest IP3Rs. Moreover, the larger d_{ERPM} at the IP_3R site, the larger the IP_3R activity (expressed as the number of opening events per IP_3R site, Fig. S16B). To better understand the mechanisms responsible for this increased activity at IP_3R sites located further away from the plasma membrane, we performed simulations in which we infused a single Ca^{2+} ion at the IP_3R site nanodomain and measured its residency time (see Methods for details on the protocol). We observed that mean Ca^{2+} residency time decreased as d_{ERPM} increased, confirming our hypothesis that increasing d_{ERPM} increases the probability of Ca^{2+} ions to diffuse away from contact sites. Importantly, distributing IP_3Rs in clusters at ER-PM

contact sites led to an increase of IP_3R activity and of Ca^{2+} peak properties as median d_{ERPM} decreased (Fig. 5F).

Overall, our results suggest that IP_3R sites close to the plasma membrane are characterized by a restricted signal diffusion to neighboring IP_3R sites, which can reduce or boost Ca^{2+} activity depending on the absence or presence of IP3R clusters, respectively. Our results thus nuance the view of ER-PM contact sites as local amplifiers of Ca^{2+} activity, conditioning this effect to the presence of clusters of Ca^{2+} channels.

4 Discussion

Here, we reconstructed 3D meshes of tripartite synapses from an isotropic high-resolution 220 μm^3 hippocampal stratum radiatum EM dataset [51]. Quantitative analysis of those meshes highlighted the diverse geometrical properties of PAPs within a single astrocyte and revealed, contrary to a widespread assumption that PAPs are devoid of ER [48, 25, 49], that 75 % of PAPs contained some ER in this dataset. We found that PAPs were closer to the PSD when bouton surface area was low, which could result from the spatial constraints imposed by larger boutons, preventing the PAP from getting in close contact to the PSD. We observed that PAPs were closer to larger boutons and larger spines. Bouton volume is correlated with the number of pre-synaptic vesicles [67] and with the size of the active zone and the latter scales with release probability [68]. Spine head volume also correlates with the number of presynaptic vesicles anchored [69]. Thus, our data suggest that PAPs might be closer to spines and boutons of more active synapses. Our data further suggest that the ER is distributed closer to the plasma membrane

in PAPs connected to larger boutons and thus more active synapses, which could, according to our simulations, impact Ca^{2+} microdomain signaling in the PAP and thus neuron-astrocyte communication. Future studies on the astrocyte nano-architecture will be important to test whether these features, observed in a single astrocyte of the CA1 region, differ with intra- and inter-regional astrocyte heterogeneity, in different physiological conditions, and in different species.

Reaction-diffusion simulations in the realistic PAP 3D meshes reconstructed in this study provided key insights into the effect of the diverse shapes and distributions of the ER observed in PAPs on microdomain Ca^{2+} activity. Notably, we reported that larger $SVR_{ER/PAP}$ triggered increases in IP_3R opening frequency and Ca^{2+} peak frequency. This could be due to intracellular diffusional barriers resulting from larger intracellular compartments, similarly to diffusional barriers mediated by the spongiform morphology of PAPs as reported previously [70]. Moreover, our simulations suggest that a distribution of the ER further away from the plasma membrane can amplify peak frequency in the absence of IP_3R clustering. Our results suggest that this effect results from an increased probability of Ca^{2+} ions released at an open IP_3R to reach a new IP_3R channel. This is due to a decreased distance between adjacent IP_3Rs and a decreased Ca^{2+} residency time when the ER is further away from the plasma membrane. Importantly, we show that the effect of the spatial distribution of the ER on Ca^{2+} dynamics strongly depends on the spatial distribution of IP_3Rs, in particular their organization into clusters at ER-PM contact sites, as reported in HeIA cells [71]. Future work studying the spatial distribution of IP_3Rs in PAPs will thus be crucial to better understand the mechanisms regulating Ca^{2+}

activity at tripartite synapses.

As reactive astrocytes, hallmark of brain diseases [72], are characterized by a remodelling of ER volume and shape [73], our results suggest that such geometrical remodeling of the ER could contribute to the altered astrocytic Ca^{2+} activity reported in pathological conditions [74].

Combining our detailed biophysical model of Ca^{2+} signals in PAPs, the PAP meshes that we reconstructed from EM, and the PAP meshes with various ER distributions produced by our automated mesh generator allowed us to fine-tune the spatial distribution of Ca^{2+} channels, monitor IP_3R opening events at individual channels, while independently manipulating ER shape and distribution, providing new insights into some mechanisms governing Ca^{2+} signaling in PAPs. Notably, we predict how the ratio between ER surface area and PAP volume, and the spatial distribution of the ER shape Ca^{2+} microdomain signals at tripartite synapses. This study is the first to our knowledge to model Ca^{2+} activity in astrocytes within realistic shapes in 3D at the nanoscale that accounts for the complex and diverse spatial characteristics of Ca^{2+} stores in PAPs and shows how small differences in the 3D intracellular landscape such as the spatial distribution of the ER, can shape local signaling. Historically, modeling studies on PAPs, including our own, have been conducted in 1D, 2D, or in simple 3D shapes, such as cylinders [54, 70, 75, 76, 77, 78]. The 3D meshes provided by this study and the algorithm generating 3D PAP meshes with various ER distributions with constant shape and size pave the way for future modeling studies to investigate the mechanisms governing neuron-astrocyte communication at tripartite synapses.

The ultrastructural data presented in this study were reconstructed from 3D FIB-SEM electron microscopy, whose tissue processing protocol, in particular the chemical fixation, might not preserve adequately the extracellular space volume, and might alter the shape of fine astrocytic structures [79]. Importantly, this technique provides a static view of the ultrastructural properties of the tissue as it cannot be used to study live cells. However, EM provides the highest spatial resolution (6 nm isotropic here) to determine PAP and ER shape to date. The exact ultrastructure of the astrocytic ER in live tissue and the physiological relevance of the ER discontinuities sometimes observed in 3D reconstructions from EM in small sub-cellular compartments, such as the astrocytic ER of this dataset, are still unclear. *In vivo* and *in vitro* super-resolution studies have recently revealed that neuronal ER is continuous in healthy conditions [80, 81, 82] and undergoes rapid fission under cerebral ischemic conditions [83] or preceding excitotoxic cell death [84]. Recently, studies have shown that this apparent continuity results from a balance between fast fission and fusion events of the ER in dendritic spines *in vitro* [85] as well as *in vivo*, following somatosensory stimulation [81]. Interestingly, cortical spreading depolarization, which causes migraine aura, also triggers widespread ER fission *in vivo* [81]. Those results highlight the plasticity of the ER shape in neurons in live tissue. Whether such fission events occur in astrocytes and their potential contribution to astrocyte function remains to be uncovered. By generating 3D meshes with various ER splitting and scattering characteristics, the algorithm developed in this study could be used to replicate different scenarios of ER fission and investigate their effect on cellular activity under (patho-)physiological conditions, although here we have simply used it as a tool to infer the

causal link between the distribution of the ER and the spatio-temporal properties of Ca^{2+} signals independently from other spatial properties.

The model used in this study describes in details the kinetics of ER-mediated Ca^{2+} signals while simplifying other Ca^{2+} sources and channels, such as mitochondria, the Na^{+}/Ca^{2+} exchanger, transient receptor potential ankyrin 1 channels and L-type voltage gated channels [29, 47]. The model is therefore well-suited to study the effect of ER shape and distribution on Ca^{2+} activity but does not allow to study other astrocytic Ca^{2+} pathways. According to our predictions, the spatial distribution of Ca^{2+} channels can alter the spatio-temporal properties of Ca^{2+} microdomain signals in PAPs. Additional quantification of the Ca^{2+} channels expressed in PAPs, their density, location in live tissue, and the remodeling of these properties under (patho-)physiological conditions will thus be essential to better understand neuron-astrocyte communication at synapses. The recent advances in super-resolution techniques, notably single-particle tracking methods, provide a promising avenue to overcome current limitations in obtaining such data [23, 86]. Another approximation of the model is that endogenous buffers are not explicitly described. The effect of Ca^{2+} buffering on cytosolic Ca^{2+} dynamics is well documented [87]. Notably, their binding to Ca^{2+} ions results in a decreased diffusion distance of free Ca^{2+} ions [88]. Thus, for simplicity, this model describes the effect of buffers with a decreased effective diffusion coefficient of free Ca^{2+} ions. In the original study presenting the model, we showed that there was no significant difference between simulations with fast Ca^{2+} diffusion and slow explicit buffers and the model with an effectively reduced Ca^{2+} diffusion coefficient (Fig. S1 of Denizot et

al. [54]). In accordance with previous reports [54, 89], our results highlight how Ca^{2+} indicators such as GCaMP, act as Ca^{2+} buffers and influence Ca^{2+} dynamics, notably increasing signal duration and decreasing peak frequency and amplitude. The local buffer concentrations dictate the decay of Ca^{2+} peaks. Buffers differ in their affinity, binding/unbinding to Ca^{2+} rates, and diffusional properties. Future research on astrocyte buffering capacity and buffer expression at the sub-cellular scale in various (patho-)physiological conditions will thus be essential to fully understand the regulation of astrocytic Ca^{2+} dynamics and homeostasis by Ca^{2+} buffers.

Here, we used a FIB-SEM dataset in the hippocampal CA1 stratum radiatum to analyze the 3D structure of tripartite synapses and of the ER inside perisynaptic astrocytic processes. It is important to note that the high resolution of the dataset (6 nm isotropic voxel size) allowed to reconstruct only a portion of a single astrocyte. Moreover, astrocyte morphology is highly complex, nanoscopic, dynamic, and diverse [90], so that the results presented in this study might not be generalizable. Recent pioneering vEM studies have started to unravel the organizing principles of astrocyte structure [63, 90, 91, 92]. Future research will be instrumental to characterize the ultrastructural properties of multipartite synapses in various species, brain regions, developmental stages, and pathological conditions, to determine the fundamental structural principles of astrocytes at the nanoscale. Such data will be crucial to increase our understanding of the now well-established astrocyte inter- and intra-cellular heterogeneity [93, 94, 95, 96] in health and disease. Acquiring and analyzing such high-resolution datasets is challenging and will

require interdisciplinary efforts to develop novel computational and computer vision tools tailored to astrocytes to facilitate their segmentation, structural analysis, and data storage [97, 98]. Combining these insights into astrocyte structure with functional studies, for example using volume correlative light-electron microscopy [99], will contribute to increasing our understanding of the roles of astrocyte morphology.

Overall, this study provides new insights into astrocyte function at tripartite synapses by characterizing the shape and distribution of the ER in PAPs of an astrocyte in the hippocampal CA1 stratum radiatum and by shedding light into the mechanistic link between those features and microdomain Ca^{2+} activity at tripartite synapses. Notably, most PAPs in this dataset contained some ER. *In silico* experiments showed that the ER surface to PAP volume ratio, the spatial distribution of the ER within PAPs, and IP_3R clustering finely regulate Ca^{2+} microdomain activity. The realistic 3D meshes of tripartite synapses provided in this study pave the way for new modeling studies of neuron-astrocyte communication in the synaptic micro-environment, allowing the study of various processes, such as glutamate spillover or gliotransmission. Such studies will be crucial to decipher whether the various nano-architectures displayed by tripartite synapses reflect distinct functional identities.

References

[1] A. Verkhratsky and M. Nedergaard, “Physiology of Astroglia,” *Physiological Reviews*, vol. 98, pp. 239–389, Jan. 2018.

[2] C. Murphy-Royal, S. Ching, and T. Papouin, “A conceptual framework for astrocyte function,” *Nature Neuroscience*, pp. 1–9,

Oct. 2023. Publisher: Nature Publishing Group.

[3] K. A. Lyon and N. J. Allen, “From Synapses to Circuits, Astrocytes Regulate Behavior,” *Frontiers in Neural Circuits*, vol. 15, 2022.

[4] A. Araque, V. Parpura, R. P. Sanzgiri, and P. G. Haydon, “Tripartite synapses: glia, the unacknowledged partner,” *Trends in Neurosciences*, vol. 22, pp. 208–215, May 1999.

[5] I. Savtchouk and A. Volterra, “Gliotransmission: Beyond Black-and-White,” *Journal of Neuroscience*, vol. 38, pp. 14–25, Jan. 2018.

[6] E. A. Bushong, M. E. Martone, Y. Z. Jones, and M. H. Ellisman, “Protoplasmic astrocytes in CA1 stratum radiatum occupy separate anatomical domains,” *The Journal of Neuroscience: The Official Journal of the Society for Neuroscience*, vol. 22, pp. 183–192, Jan. 2002.

[7] M. R. Witcher, S. A. Kirov, and K. M. Harris, “Plasticity of perisynaptic astroglia during synaptogenesis in the mature rat hippocampus,” *Glia*, vol. 55, pp. 13–23, Jan. 2007.

[8] I. Lushnikova, G. Skibo, D. Muller, and I. Nikonenko, “Synaptic potentiation induces increased glial coverage of excitatory synapses in CA1 hippocampus,” *Hippocampus*, vol. 19, pp. 753–762, Aug. 2009.

[9] M. K. Herde, K. Bohmbach, C. Domingos, N. Vana, J. A. Komorowska-Müller, S. Passlick, I. Schwarz, C. J. Jackson, D. Dietrich, M. K. Schwarz, and C. Henneberger, “Local Efficacy of Glutamate Uptake Decreases with Synapse Size,” *Cell Reports*, vol.

32, p. 108182, Sept. 2020.

[10] C. Henneberger, L. Bard, A. Panatier, J. P. Reynolds, O. Kopach, N. I. Medvedev, D. Minge, M. K. Herde, S. Anders, I. Kraev, J. P. Heller, S. Rama, K. Zheng, T. P. Jensen, I. Sanchez-Romero, C. J. Jackson, H. Janovjak, O. P. Ottersen, E. A. Nagelhus, S. H. R. Oliet, M. G. Stewart, U. V. Nägerl, and D. A. Rusakov, "LTP Induction Boosts Glutamate Spillover by Driving Withdrawal of Perisynaptic Astroglia," *Neuron*, vol. 108, pp. 919–936.e11, Dec. 2020.

[11] A. Badia-Soteras, T. S. Heistek, M. Kater, A. Negrean, H. S. Mansvelder, B. Khakh, R. Min, A. Smit, and M. Verheijen, "Proximity of astrocyte leaflets to the synapse determines memory strength," tech. rep., bioRxiv, Jan. 2022. Section: New Results Type: article.

[12] A. Reichenbach, A. Derouiche, and F. Kirchhoff, "Morphology and dynamics of perisynaptic glia," *Brain Research Reviews*, vol. 63, pp. 11–25, May 2010.

[13] Y. Bernardinelli, J. Randall, E. Janett, I. Nikonenko, S. Konig, E. V. Jones,¨ C. E. Flores, K. K. Murai, C. G. Bochet, A. Holtmaat, and D. Muller,
"Activity-dependent structural plasticity of perisynaptic astrocytic domains promotes excitatory synapse stability," *Current biology: CB*, vol. 24, pp. 1679–1688, Aug. 2014.

[14] A. Verkhratsky and M. Nedergaard, "Astroglial cradle in the life of the synapse," *Philosophical Transactions of the Royal Society B: Biological Sciences*, vol. 369, Oct. 2014.

[15] A. Araque, G. Carmignoto, P. G. Haydon, S. H. R. Oliet, R. Robitaille,

and A. Volterra, “Gliotransmitters travel in time and space,” *Neuron*, vol. 81, pp. 728–739, Feb. 2014.

[16] N. Mazaré, M. Oudart, J. Moulard, G. Cheung, R. Tortuyaux, P. Mailly,´D. Mazaud, A.-P. Bemelmans, A.-C. Boulay, C. Blugeon, L. Jourdren, S. Le Crom, N. Rouach, and M. Cohen-Salmon, “Local Translation in Perisynaptic Astrocytic Processes Is Specific and Changes after Fear Conditioning,” *Cell Reports*, vol. 32, p. 108076, Aug. 2020.

[17] J. B. Foster, F. Zhao, X. Wang, Z. Xu, K. Lin, C. C. Askwith, K. J. Hodgetts, and C.-L. Glenn Lin, “Pyridazine-derivatives enhance structural and functional plasticity of tripartite synapse via activation of local translation in astrocytic processes,” *Neuroscience*, July 2018.

[18] L. E. Ostroff, M. K. Manzur, C. K. Cain, and J. E. LeDoux, “Synapses lacking astrocyte appear in the amygdala during consolidation of Pavlovian threat conditioning,” *The Journal of comparative neurology*, vol. 522, pp. 2152–2163, June 2014.

[19] A. Panatier, D. T. Theodosis, J.-P. Mothet, B. Touquet, L. Pollegioni, D. A. Poulain, and S. H. R. Oliet, “Glia-Derived d-Serine Controls NMDA Receptor Activity and Synaptic Memory,” *Cell*, vol. 125, pp. 775–784, May
2006.

[20] A. Perez-Alvarez, M. Navarrete, A. Covelo, E. D. Martin, and A. Araque, “Structural and functional plasticity of astrocyte processes and dendritic spine interactions,” *The Journal of Neuroscience: The*

Official Journal of the Society for Neuroscience, vol. 34, pp. 12738–12744, Sept. 2014.

[21] C. Genoud, C. Quairiaux, P. Steiner, H. Hirling, E. Welker, and G. W. Knott,
"Plasticity of Astrocytic Coverage and Glutamate Transporter Expression in Adult Mouse Cortex," *PLoS Biology*, vol. 4, p. e343, Oct. 2006.

[22] J. Wenzel, G. Lammert, U. Meyer, and M. Krug, "The influence of long-term potentiation on the spatial relationship between astrocyte processes and potentiated synapses in the dentate gyrus neuropil of rat brain," *Brain Research*, vol. 560, pp. 122–131, Sept. 1991.

[23] J. P. Heller and D. A. Rusakov, "The Nanoworld of the Tripartite Synapse: Insights from Super-Resolution Microscopy," *Frontiers in Cellular Neuroscience*, vol. 11, 2017.

[24] M. Arizono, V. V. G. K. Inavalli, S. Bancelin, M. Fernandez-Monreal,´ and U. V. Nagerl, "Super-resolution shadow imaging reveals local remod-¨ eling of astrocytic microstructures and brain extracellular space after osmotic challenge," *Glia*, vol. 69, no. 6, pp. 1605–1613, 2021. eprint:
https://onlinelibrary.wiley.com/doi/pdf/10.1002/glia.23995.

[25] D. A. Rusakov, "Disentangling calcium-driven astrocyte physiology," *Nature Reviews Neuroscience*, vol. 16, pp. 226–233, Apr. 2015.

[26] A. Aboufares El Alaoui, M. Jackson, M. Fabri, L. de Vivo, and M. Bellesi, "Characterization of Subcellular Organelles in Cortical

Perisynaptic Astrocytes," *Frontiers in Cellular Neuroscience*, vol. 14, 2021. Publisher: Fron-
tiers.

[27] A. Verkhratsky, A. Semyanov, and R. Zorec, "Physiology of Astroglial Excitability," *Function*, vol. 1, Sept. 2020.

[28] A. Semyanov, C. Henneberger, and A. Agarwal, "Making sense of astrocytic calcium signals — from acquisition to interpretation," *Nature Reviews Neuroscience*, vol. 21, pp. 551–564, Oct. 2020. Number: 10 Publisher: Nature Publishing Group.

[29] E. Shigetomi, S. Patel, and B. S. Khakh, "Probing the Complexities of Astrocyte Calcium Signaling," *Trends in Cell Biology*, vol. 26, pp. 300–312, Apr. 2016.

[30] A. Lia, V. J. Henriques, M. Zonta, A. Chiavegato, G. Carmignoto, M. Gómez-Gonzalo, and G. Losi, "Calcium Signals in Astrocyte Mi-´ crodomains, a Decade of Great Advances," *Frontiers in Cellular Neuroscience*, vol. 15, 2021. Publisher: Frontiers.

[31] L. Georgiou, A. Echeverría, A. Georgiou, and B. Kuhn, "Ca+ activity maps of astrocytes tagged by axoastrocytic AAV transfer," *Science Advances*, vol. 8, no. 6, p. eabe5371, 2022. Publisher: American Association for the
Advancement of Science.

[32] A. Agarwal, P.-H. Wu, E. G. Hughes, M. Fukaya, M. A. Tischfield, A. J. Langseth, D. Wirtz, and D. E. Bergles, "Transient Opening of the Mitochondrial Permeability Transition Pore Induces Microdomain

Calcium Transients in Astrocyte Processes," *Neuron*, vol. 93, pp. 587–605.e7, Feb. 2017.

[33] E. Bindocci, I. Savtchouk, N. Liaudet, D. Becker, G. Carriero, and A. Volterra, "Three-dimensional Ca^{2+} imaging advances understanding of astrocyte biology," *Science*, vol. 356, p. eaai8185, May 2017.

[34] A. Asada, S. Ujita, R. Nakayama, S. Oba, S. Ishii, N. Matsuki, and Y. Ikegaya, "Subtle modulation of ongoing calcium dynamics in astrocytic microdomains by sensory inputs," *Physiological Reports*, vol. 3, Oct. 2015.

[35] E. Shigetomi, E. A. Bushong, M. D. Haustein, X. Tong, O. Jackson-Weaver, S. Kracun, J. Xu, M. V. Sofroniew, M. H. Ellisman, and B. S. Khakh, "Imaging calcium microdomains within entire astrocyte territories and endfeet with GCaMPs expressed using adeno-associated viruses," *The Journal of General Physiology*, vol. 141, pp. 633–647, May 2013.

[36] M.-Y. Sun, P. Devaraju, A. X. Xie, I. Holman, E. Samones, T. R. Murphy, and T. A. Fiacco, "Astrocyte calcium microdomains are inhibited by Bafilomycin A1 and cannot be replicated by low-level Schaffer collateral stimulation in situ," *Cell Calcium*, vol. 55, pp. 1–16, Jan. 2014.

[37] J. L. Stobart, K. D. Ferrari, M. J. P. Barrett, C. Gluck, M. J. Stobart, M. Zuend, and B. Weber, "Cortical Circuit Activity Evokes Rapid Astrocyte Calcium Signals on a Similar Timescale to Neurons," *Neuron*, vol. 98, pp. 726–735.e4, May 2018.

[38] R. Srinivasan, B. S. Huang, S. Venugopal, A. D. Johnston, H. Chai, H. Zeng, P. Golshani, and B. S. Khakh, “Ca(2+) signaling in astrocytes from Ip3r2(/-) mice in brain slices and during startle responses in vivo,” *Nature Neuroscience*, vol. 18, pp. 708–717, May 2015.

[39] M. W. Sherwood, M. Arizono, C. Hisatsune, H. Bannai, E. Ebisui, J. L. Sherwood, A. Panatier, S. H. R. Oliet, and K. Mikoshiba, “Astrocytic IP3Rs: Contribution to Ca2+ signalling and hippocampal LTP,” *Glia*, vol. 65, pp. 502–513, Mar. 2017.

[40] A. Panatier, J. Vallee, M. Haber, K. K. Murai, J.-C. Lacaille, and R. Robitaille, “Astrocytes are endogenous regulators of basal transmission at central synapses,” *Cell*, vol. 146, pp. 785–798, Sept. 2011.

[41] M. A. Di Castro, J. Chuquet, N. Liaudet, K. Bhaukaurally, M. Santello, D. Bouvier, P. Tiret, and A. Volterra, “Local Ca2+ detection and modulation of synaptic release by astrocytes,” *Nature Neuroscience*, vol. 14, pp. 1276– 1284, Oct. 2011.

[42] B. L. Lind, A. R. Brazhe, S. B. Jessen, F. C. C. Tan, and M. J. Lauritzen, “Rapid stimulus-evoked astrocyte Ca2+ elevations and hemodynamic responses in mouse somatosensory cortex in vivo,” *Proceedings of the National Academy of Sciences*, p. 201310065, Nov. 2013.

[43] A. Panatier, M. Arizono, and U. V. Nägerl, “Dissecting tripartite synapses with STED microscopy,” *Phil. Trans. R. Soc. B*, vol. 369, p. 20130597, Oct. 2014.

[44] M. Arizono, V. V. G. K. Inavalli, A. Panatier, T. Pfeiffer, J. Angibaud, F. Levet, M. J. T. T. Veer, J. Stobart, L. Bellocchio, K. Mikoshiba, G. Marsicano, B. Weber, S. H. R. Oliet, and U. V. Nägerl, “Structural basis of astrocytic Ca 2+ signals at tripartite synapses,” *Nature Communications*, vol. 11, pp. 1–15, Apr. 2020. Publisher: Nature Publishing Group.

[45] C. Calì, J. Lopatar, F. Petrelli, L. Pucci, and P. Bezzi, “G-Protein Coupled Receptor-Evoked Glutamate Exocytosis from Astrocytes: Role of Prostaglandins,” *Neural Plasticity*, vol. 2014, p. e254574, Jan. 2014. Publisher: Hindawi.

[46] J. Marchaland, C. Calì, S. M. Voglmaier, H. Li, R. Regazzi, R. H. Edwards, and P. Bezzi, “Fast Subplasma Membrane Ca2+ Transients Control ExoEndocytosis of Synaptic-Like Microvesicles in Astrocytes,” *Journal of Neuroscience*, vol. 28, pp. 9122–9132, Sept. 2008.

[47] M. W. Sherwood, M. Arizono, A. Panatier, K. Mikoshiba, and S. H. R. Oliet, “Astrocytic IP3Rs: Beyond IP3R2,” *Frontiers in Cellular Neuroscience*, vol. 0, 2021. Publisher: Frontiers.

[48] I. Patrushev, N. Gavrilov, V. Turlapov, and A. Semyanov, “Subcellular location of astrocytic calcium stores favors extrasynaptic neuron-astrocyte communication,” *Cell Calcium*, vol. 54, pp. 343–349, Nov. 2013.

[49] A. Semyanov and A. Verkhratsky, “Astrocytic processes: from tripartite synapses to the active milieu,” *Trends in Neurosciences*, vol. 44, pp. 781– 792, Oct. 2021.

[50] L. H. Bergersen, C. Morland, L. Ormel, J. E. Rinholm, M. Larsson, J. F. H. Wold, A. T. Roe, A. Stranna, M. Santello, D. Bouvier, O. P. Ottersen, A. Volterra, and V. Gundersen, “Immunogold Detection of L-glutamate and D-serine in Small Synaptic-Like Microvesicles in Adult Hippocampal Astrocytes,” *Cerebral Cortex*, vol. 22, pp. 1690–1697, July 2012.

[51] C. Calì, J. Baghabra, D. J. Boges, G. R. Holst, A. Kreshuk, F. A. Hamprecht, M. Srinivasan, H. Lehvaslaiho, and P. J. Magistretti, “Three-dimensional¨ immersive virtual reality for studying cellular compartments in 3D models from EM preparations of neural tissues,” *Journal of Comparative Neurology*, vol. 524, pp. 23–38, Jan. 2016.

[52] C. Calì, K. Kare, M. Agus, M. F. V. Castillo, D. Boges, M. Hadwiger, and P. Magistretti, “A Method for 3D Reconstruction and Virtual Reality Analysis of Glial and Neuronal Cells,” *JoVE (Journal of Visualized Experiments)*,
p. e59444, Sept. 2019.

[53] Y. Hu, Q. Zhou, X. Gao, A. Jacobson, D. Zorin, and D. Panozzo, “Tetrahedral meshing in the wild,” *ACM Transactions on Graphics*, vol. 37, pp. 60:1– 60:14, July 2018.

[54] A. Denizot, M. Arizono, U. V. Nägerl, H. Soula, and H. Berry, “Simulation of calcium signaling in fine astrocytic processes: Effect of spatial properties on spontaneous activity,” *PLOS Computational Biology*, vol. 15, p. e1006795, Aug. 2019.

[55] G. W. De Young and J. Keizer, “A single-pool inositol 1,4,5-trisphosphatereceptor-based model for agonist-stimulated oscillations in Ca2+ concentration.,” *Proceedings of the National*

Academy of Sciences, vol. 89, pp. 9895– 9899, Oct. 1992.

[56] N. L. Allbritton, T. Meyer, and L. Stryer, “Range of messenger action of calcium ion and inositol 1,4,5-trisphosphate,” Science (New York, N.Y.), vol. 258, pp. 1812–1815, Dec. 1992.

[57] I. Hepburn, W. Chen, S. Wils, and E. De Schutter, “STEPS: efficient simulation of stochastic reaction–diffusion models in realistic morphologies,” *BMC Systems Biology*, vol. 6, no. 1, p. 36, 2012.

[58] I. Hepburn, W. Chen, and E. De Schutter, “Accurate reaction-diffusion operator splitting on tetrahedral meshes for parallel stochastic molecular simulations,” *The Journal of Chemical Physics*, vol. 145, p. 054118, Aug. 2016.

[59] D. T. Gillespie, “Exact stochastic simulation of coupled chemical reactions,” *The Journal of Physical Chemistry*, vol. 81, pp. 2340–2361, Dec. 1977.

[60] D. Meyer, T. Bonhoeffer, and V. Scheuss, “Balance and Stability of Synaptic Structures during Synaptic Plasticity,” *Neuron*, vol. 82, pp. 430–443, Apr. 2014.

[61] C. Calì, M. Wawrzyniak, C. Becker, B. Maco, M. Cantoni, A. Jorstad, B. Nigro, F. Grillo, V. D. Paola, P. Fua, and G. W. Knott, “The effects of aging on neuropil structure in mouse somatosensory cortex—A 3D electron microscopy analysis of layer 1,” PLOS ONE, vol. 13, p. e0198131, July 2018. Publisher: Public Library of Science.

[62] N. Medvedev, V. Popov, C. Henneberger, I. Kraev, D. A. Rusakov, and M. G. Stewart, “Glia selectively approach synapses on thin

dendritic spines," *Phil. Trans. R. Soc. B*, vol. 369, p. 20140047, Oct. 2014.

[63] S. Aten, C. M. Kiyoshi, E. P. Arzola, J. A. Patterson, A. T. Taylor, Y. Du, A. M. Guiher, M. Philip, E. G. Camacho, D. Mediratta, K. Collins, K. Boni, S. A. Garcia, R. Kumar, A. N. Drake, A. Hegazi, L. Trank, E. Benson, G. Kidd, D. Terman, and M. Zhou, "Ultrastructural view of astrocyte arborization, astrocyte-astrocyte and astrocyte-synapse contacts, intracellular vesicle-like structures, and mitochondrial network," Progress in Neurobiology, vol. 213, p. 102264, June 2022.

[64] I. Hepburn, R. Cannon, and E. De Schutter, "Efficient calculation of the quasi-static electrical potential on a tetrahedral mesh and its implementation in STEPS," *Frontiers in Computational Neuroscience*, vol. 7, Oct. 2013.

[65] "Spontaneous astrocytic calcium traces from organotypic hippocampal slices," July 2019. Publisher: figshare.

[66] S. Zeller, S. Rudiger, H. Engel, J. Sneyd, G. Warnecke, I. Parker, and M. Falcke, "Modeling of the modulation by buffers of Ca2+ release through clusters of IP3 receptors," *Biophysical Journal*, vol. 97, pp. 992–1002, Aug. 2009.

[67] A. Rollenhagen, O. Ohana, K. Sätzler, C. C. Hilgetag, D. Kuhl, and J. H. R. Lübke, "Structural Properties of Synaptic Transmission and Temporal Dynamics at Excitatory Layer 5B Synapses in the Adult Rat Somatosensory Cortex," *Frontiers in Synaptic Neuroscience*, vol. 10, 2018. Publisher: Frontiers.

[68] N. Holderith, A. Lorincz, G. Katona, B. Rózsa, A. Kulik, M.

Watanabe,´ and Z. Nusser, “Release probability of hippocampal glutamatergic terminals scales with the size of the active zone,” *Nature Neuroscience*, vol. 15, pp. 988–997, July 2012. Number: 7 Publisher: Nature Publishing Group.

[69] T. M. Bartol, Jr, C. Bromer, J. Kinney, M. A. Chirillo, J. N. Bourne, K. M. Harris, and T. J. Sejnowski, “Nanoconnectomic upper bound on the variability of synaptic plasticity,” *eLife*, vol. 4, p. e10778, Nov. 2015. Publisher: eLife Sciences Publications, Ltd.

[70] A. Denizot, M. Arizono, U. V. Nägerl, H. Berry, and E. De Schutter, “Control of Ca2+ signals by astrocyte nanoscale morphology at tripartite synapses,” *Glia*, vol. 70, no. 12, pp. 2378–2391, 2022.

[71] N. B. Thillaiappan, A. Chavda, S. Tovey, D. Prole, and C. Taylor, “Ca2+ signals initiate at immobile IP3 receptors adjacent to ER-plasma membrane junctions,” *Nature Communications*, vol. 8, Dec. 2017.

[72] C. Escartin, E. Galea, A. Lakatos, J. P. O’Callaghan, G. C. Petzold, A. Serrano-Pozo, C. Steinhauser, A. Volterra, G. Carmignoto, A. Agarwal, N. J. Allen, A. Araque, L. Barbeito, A. Barzilai, D. E. Bergles, G. Bonvento, A. M. Butt, W.-T. Chen, M. Cohen-Salmon, C. Cunningham, B. Deneen, B. De Strooper, B. Díaz-Castro, C. Farina, M. Freeman, V. Gallo, J. E. Goldman, S. A. Goldman, M. Götz, A. Gutiérrez, P. G. Haydon, D. H. Heiland,´ E. M. Hol, M. G. Holt, M. Iino, K. V. Kastanenka, H. Kettenmann, B. S. Khakh, S. Koizumi, C. J. Lee, S. A. Liddelow, B. A. MacVicar, P. Magistretti, A. Messing, A. Mishra, A. V. Molofsky, K. K. Murai, C. M. Norris, S. Okada, S. H. R.

Oliet, J. F. Oliveira, A. Panatier, V. Parpura, M. Pekna, Pekny, L. Pellerin, G. Perea, B. G. Pérez-Nievas, F. W. Pfrieger, K. E.´ Poskanzer, F. J. Quintana, R. M. Ransohoff, M. Riquelme-Perez, S. Robel, C. R. Rose, J. D. Rothstein, N. Rouach, D. H. Rowitch, A. Semyanov, S. Sirko, H. Sontheimer, R. A. Swanson, J. Vitorica, I.-B. Wanner, L. B. Wood, J. Wu, B. Zheng, E. R. Zimmer, R. Zorec, M. V. Sofroniew, and A. Verkhratsky, "Reactive astrocyte nomenclature, definitions, and future directions," *Nature Neuroscience*, pp. 1–14, Feb. 2021. Publisher: Nature Publishing Group.

[73] J. R. Jones, L. Kong, M. G. Hanna, B. Hoffman, R. Krencik, R. Bradley, T. Hagemann, J. Choi, M. Doers, M. Dubovis, M. A. Sherafat, A. Bhattacharyya, C. Kendziorski, A. Audhya, A. Messing, and S.-C. Zhang, "Mutations in GFAP Disrupt the Distribution and Function of Organelles in Human Astrocytes," *Cell Reports*, vol. 25, pp. 947–958.e4, Oct. 2018.

[74] E. Shigetomi, K. Saito, F. Sano, and S. Koizumi, "Aberrant Calcium Signals in Reactive Astrocytes: A Key Process in Neurological Disorders," *International Journal of Molecular Sciences*, vol. 20, p. 996, Jan. 2019.

[75] T. Manninen, R. Havela, and M.-L. Linne, "Computational Models for Calcium-Mediated Astrocyte Functions," *Frontiers in Computational Neuroscience*, vol. 12, Apr. 2018.

[76] A. Denizot, H. Berry, and S. Venugopal, "Intracellular Calcium Signals in Astrocytes, Computational Modeling of," in *Encyclopedia of Computational Neuroscience* (D. Jaeger and R. Jung, eds.), pp. 1–12, New York, NY: Springer, 2020.

[77] K. Breslin, J. J. Wade, K. Wong-Lin, J. Harkin, B. Flanagan, H. V. Zalinge, S. Hall, M. Walker, A. Verkhratsky, and L. McDaid, “Potassium and sodium microdomains in thin astroglial processes: A computational model study,” *PLOS Computational Biology*, vol. 14, p. e1006151, May 2018.

[78] L. Héja, Z. Szabó, M. Péter, and J. Kardos, “Spontaneous Ca2+ Fluctuations´ Arise in Thin Astrocytic Processes With Real 3D Geometry,” *Frontiers in Cellular Neuroscience*, vol. 15, 2021. Publisher: Frontiers.

[79] N. Korogod, C. C. Petersen, and G. W. Knott, “Ultrastructural analysis of adult mouse neocortex comparing aldehyde perfusion with cryo fixation,” *eLife*, vol. 4, p. e05793, 2015.

[80] T. Cui-Wang, C. Hanus, T. Cui, T. Helton, J. Bourne, D. Watson, K. Harris, and M. Ehlers, “Local Zones of Endoplasmic Reticulum Complexity Confine Cargo in Neuronal Dendrites,” *Cell*, vol. 148, pp. 309–321, Jan. 2012.

[81] K. Kucharz and M. Lauritzen, “CaMKII-dependent endoplasmic reticulum fission by whisker stimulation and during cortical spreading depolarization,” *Brain: A Journal of Neurology*, vol. 141, pp. 1049–1062, Apr. 2018.

[82] D. P. Hoffman, G. Shtengel, C. S. Xu, K. R. Campbell, M. Freeman, L. Wang, D. E. Milkie, H. A. Pasolli, N. Iyer, J. A. Bogovic, D. R. Stabley, A. Shirinifard, S. Pang, D. Peale, K. Schaefer, W. Pomp, C.-L. Chang, J. Lippincott-Schwartz, T. Kirchhausen, D. J. Solecki, E. Betzig, and H. F. Hess, “Correlative three-dimensional super-

resolution and block-face electron microscopy of whole vitreously frozen cells," *Science*, vol. 367, Jan. 2020. Publisher: American Association for the Advancement of Science Section: Research Article.

[83] T. Banno and K. Kohno, "Conformational changes of smooth endoplasmic reticulum induced by brief anoxia in rat Purkinje cells," *Journal of Comparative Neurology*, vol. 369, no. 3, pp. 462–471, 1996.

[84] K. Kucharz, M. Krogh, A. N. Ng, and H. Toresson, "NMDA Receptor Stimulation Induces Reversible Fission of the Neuronal Endoplasmic Reticulum," *PLOS ONE*, vol. 4, p. e5250, Apr. 2009. Publisher: Public Library of Science.

[85] K. V. Kuchibhotla, C. R. Lattarulo, B. T. Hyman, and B. J. Bacskai, "Synchronous Hyperactivity and Intercellular Calcium Waves in Astrocytes in Alzheimer Mice," *Science*, vol. 323, pp. 1211–1215, Feb. 2009.

[86] M. Arizono, S. Bancelin, P. Bethge, R. Chéreau, A. Idziak, V. V. G. K. Inavalli, T. Pfeiffer, J. Tønnesen, and U. V. Nägerl, "Nanoscale imaging of the functional anatomy of the brain," *Neuroforum*, vol. 27, pp. 67–77, May 2021. Publisher: De Gruyter.

[87] D. Eisner, E. Neher, H. Taschenberger, and G. Smith, "Physiology of intra-cellular calcium buffering," Physiological Reviews, vol. 103, pp. 2767–2845, Oct. 2023. Publisher: American Physiological Society

[88] S. R¨udiger, C. Nagaiah, G. Warnecke, and J. Shuai, "Calcium Domains around Single and Clustered IP3 Receptors and Their Modulation by Buffers," Biophysical Journal, vol. 99, pp. 3–12, July

2010.

[89] S. M. McMahon and M. B. Jackson, “An Inconvenient Truth: Calcium Sensors Are Calcium Buffers,” Trends in Neurosciences, vol. 41, pp. 880–884, Dec. 2018.

[90] K. T. Baldwin, K. K. Murai, and B. S. Khakh, “Astrocyte morphology,” Trends in Cell Biology, Oct. 2023.

[91] C. Calì, M. Agus, K. Kare, D. J. Boges, H. Lehvaslaiho, M. Hadwiger, and P. J. Magistretti, “3D cellular reconstruction of cortical glia and parenchymal morphometric analysis from Serial Block-Face Electron Microscopy of juvenile rat,” Progress in Neurobiology, p. 101696, Sept. 2019.

[92] C. K. Salmon, T. A. Syed, J. B. Kacerovsky, N. Alivodej, A. L. Schober, T. F. W. Sloan, M. T. Pratte, M. P. Rosen, M. Green, A. Chirgwin-Dasgupta, S. Mehta, A. Jilani, Y. Wang, H. Vali, C. A. Mandato, K. Siddiqi, and K. K. Murai, “Organizing principles of astrocytic nanoarchitecture in the mouse cerebral cortex,” Current Biology, vol. 0, Feb. 2023.

[93] L. B. Haim and D. H. Rowitch, “Functional diversity of astrocytes in neural circuit regulation,” Nature Reviews Neuroscience, vol. 18, pp. 31–41, Jan. 2017.

[94] M. Holt, “Astrocyte heterogeneity and interactions with local neural circuits,” Essays in Biochemistry, vol. 67, pp. 93–106, Mar. 2023.

[95] B. L. Clayton and S. A. Liddelow, “Heterogeneity of astrocyte reactivity,” Annual Review of Neuroscience, vol. 48, no. 1, pp. 231–249, 2025.

[96] W. Kwon, M. R. Williamson, and B. Deneen, “A functional perspective on astrocyte heterogeneity,” Trends in Neurosciences,

2025.

[97] T. A. Syed, M. Youssef, A. L. Schober, Y. Kubota, K. K. Murai, and C. K. Salmon, “Beyond neurons: computer vision methods for analysis of morphologically complex astrocytes,” Frontiers in Computer Science, vol. 6, Sept. 2024. Publisher: Frontiers.

[98] V. Chiappini, M. F. V. Castillo, F. Biancardi, F. Di Cunto, P. J. Magistretti, A. Vercelli, M. Agus, and C. Calì, “Ultrastructure of astrocytes using volume electron microscopy: A scoping review,” The Journal of Physiology, 2025.

[99] P. de Boer, J. P. Hoogenboom, and B. N. G. Giepmans, “Correlated light and electron microscopy: ultrastructure lights up!,” Nature Methods, vol. 12, pp. 503–513, June 2015.

Figure 1.

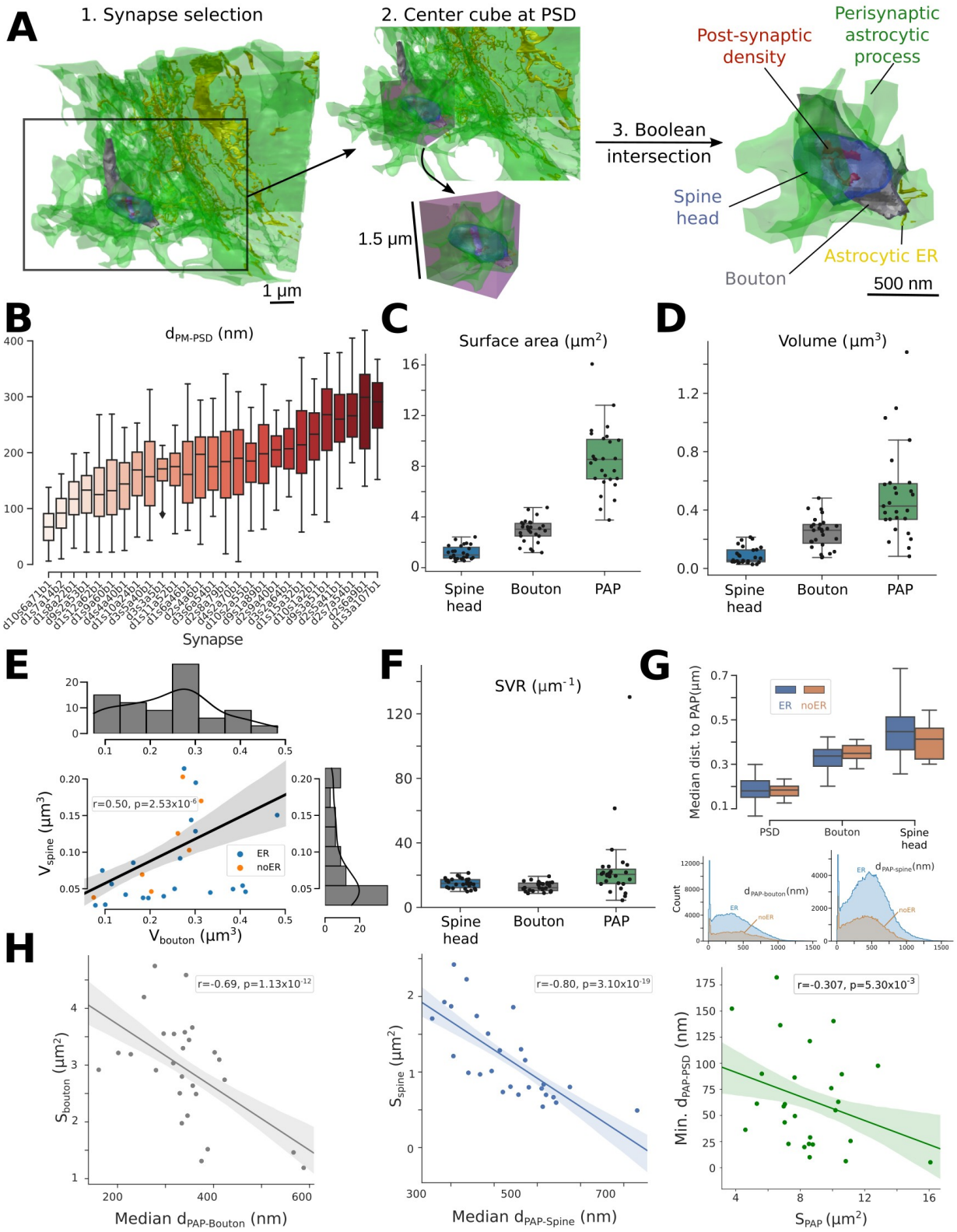
A
1. Synapse selection
2. Center cube at PSD
3. Boolean intersection
Post-synaptic density
Perisynaptic astrocytic process
Spine head
Astrocytic ER
Bouton
1 µm
1.5 µm
500 nm
B
d_{PM-PSD} (nm)
Synapse
C
Surface area (µm²)
Spine head
Bouton
PAP
D
Volume (µm³)
E
r=0.50, p=2.53x10⁻⁶
ER
noER
V_{spine} (µm³)
V_{bouton} (µm³)
F
SVR (µm⁻¹)
G
Median dist. to PAP(µm)
PSD
Count
$d_{PAP-bouton}$(nm)
$d_{PAP-spine}$(nm)
H
r=-0.69, p=1.13x10⁻¹²
S_{bouton} (µm²)
Median $d_{PAP-Bouton}$ (nm)
r=-0.80, p=3.10x10⁻¹⁹
S_{spine} (µm²)
Median $d_{PAP-Spine}$ (nm)
r=-0.307, p=5.30x10⁻³
Min. $d_{PAP-PSD}$ (nm)
S_{PAP} (µm²)

Figure 2.

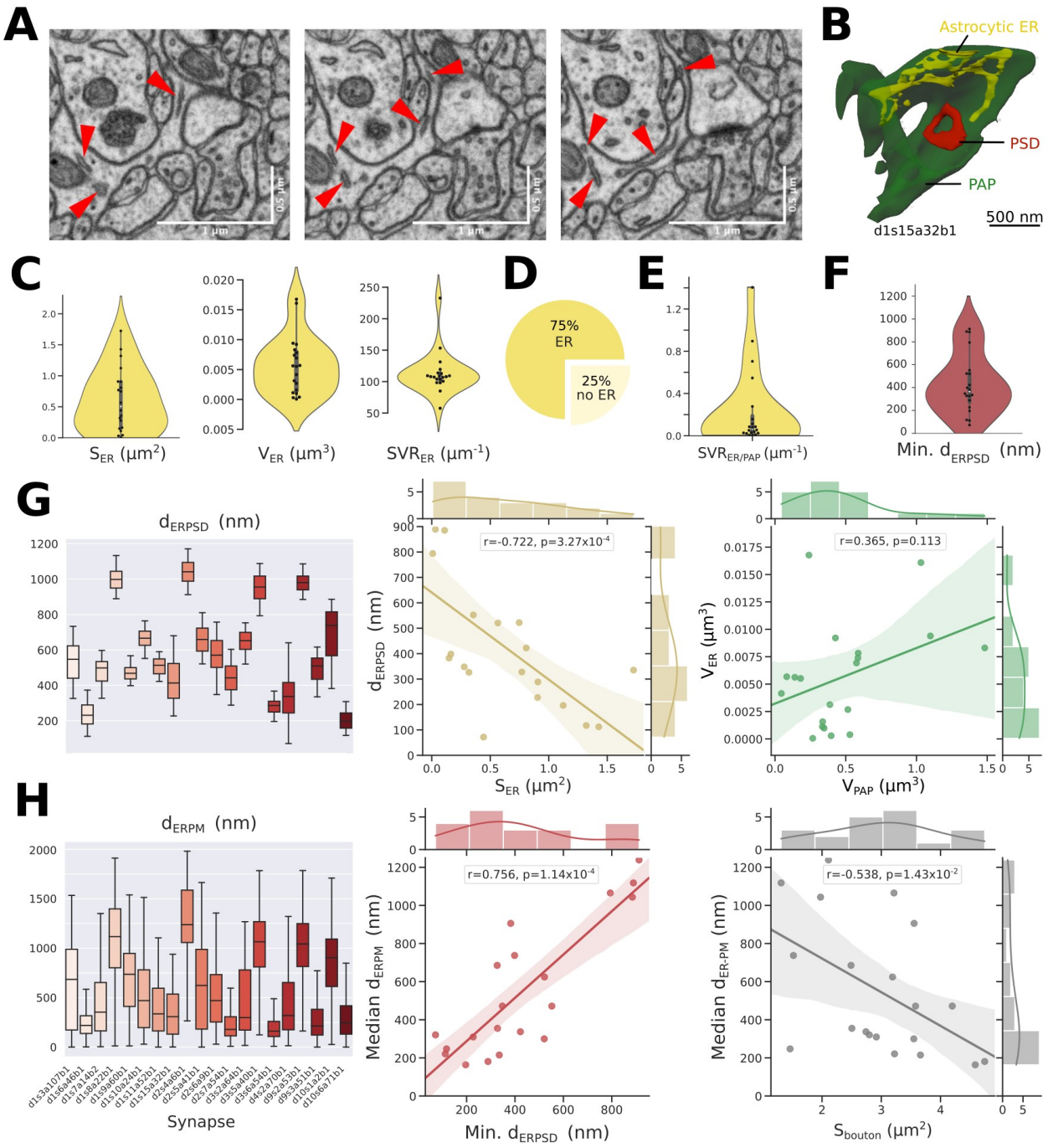
A
1 µm
0.5 µm
B
Astrocytic ER
PSD
PAP
500 nm
d1s15a32b1
C
S_{ER} (µm²)
V_{ER} (µm³)
SVR_{ER} (µm⁻¹)
D
75% ER
25% no ER
E
$SVR_{ER/PAP}$ (µm⁻¹)
F
Min. d_{ERPSD} (nm)
G
d_{ERPSD} (nm)
r=-0.722, p=3.27x10⁻⁴
d_{ERPSD} (nm)
S_{ER} (µm²)
r=0.365, p=0.113
V_{ER} (µm³)
V_{PAP} (µm³)
H
d_{ERPM} (nm)
Synapse
r=0.756, p=1.14x10⁻⁴
Median d_{ERPM} (nm)
Min. d_{ERPSD} (nm)
r=-0.538, p=1.43x10⁻²
Median d_{ER-PM} (nm)
S_{bouton} (µm²)

Figure 3.

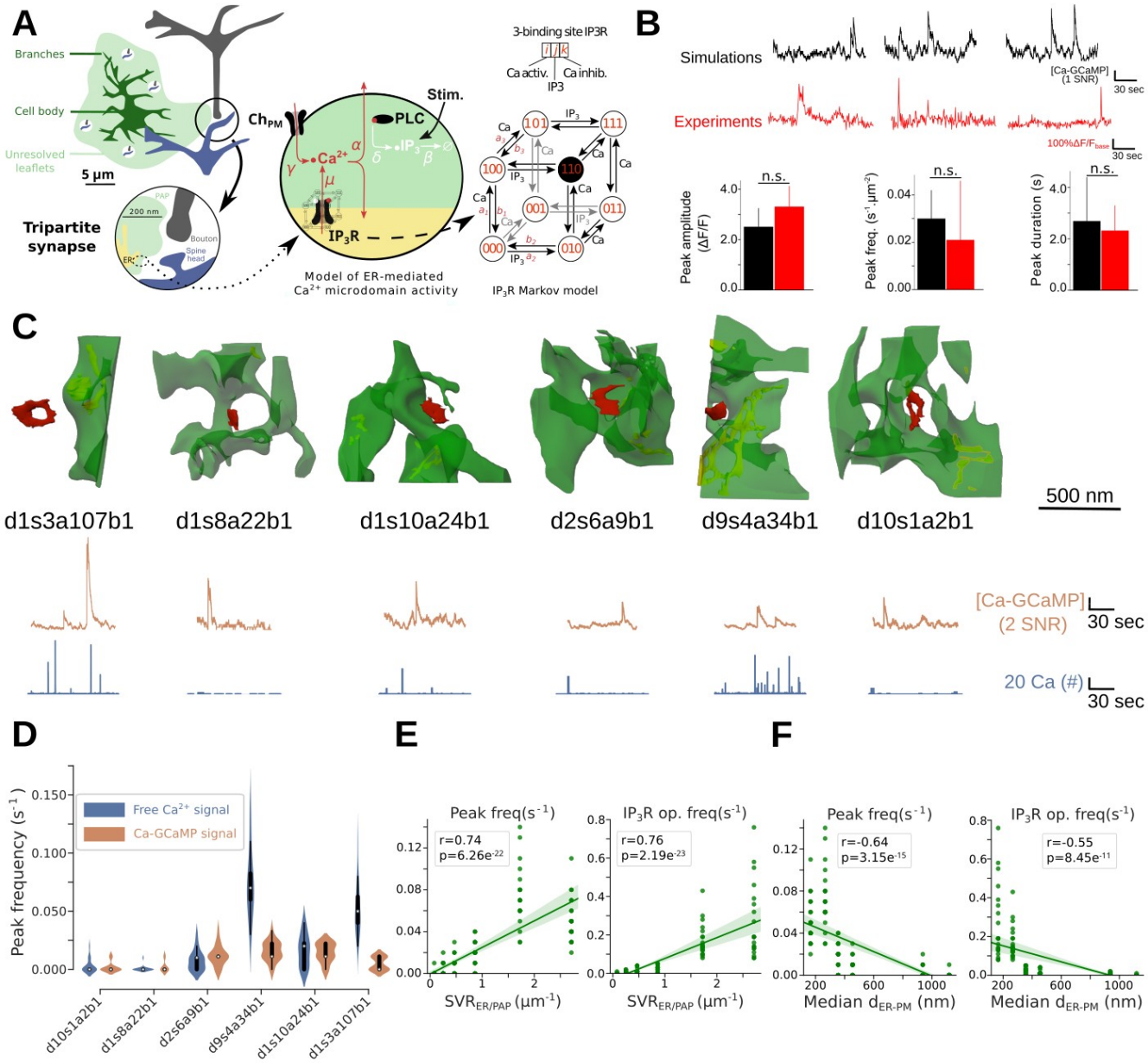
A
Branches
Cell body
Unresolved leaflets
5 µm
Tripartite synapse
200 nm
PAP
Bouton
Spine head
ER
Ch_PM
PLC
Stim.
Ca2+
IP3
IP3R
Model of ER-mediated Ca2+ microdomain activity
3-binding site IP3R
Ca activ.
Ca inhib.
IP3
IP3R Markov model
B
Simulations
Experiments
[Ca-GCaMP] (1 SNR)
30 sec
100%ΔF/F_base
Peak amplitude (ΔF/F)
Peak freq. (s-1.µm-2)
Peak duration (s)
n.s.
C
d1s3a107b1
d1s8a22b1
d1s10a24b1
d2s6a9b1
d9s4a34b1
d10s1a2b1
500 nm
[Ca-GCaMP] (2 SNR)
30 sec
20 Ca (#)
30 sec
D
Peak frequency (s-1)
Free Ca2+ signal
Ca-GCaMP signal
d10s1a2b1
d1s8a22b1
d2s6a9b1
d9s4a34b1
d1s10a24b1
d1s3a107b1
E
Peak freq(s-1)
r=0.74
p=6.26e-22
IP3R op. freq(s-1)
r=0.76
p=2.19e-23
SVR_ER/PAP (µm-1)
F
Peak freq(s-1)
r=-0.64
p=3.15e-15
IP3R op. freq(s-1)
r=-0.55
p=8.45e-11
Median d_ER-PM (nm)

Figure 4.

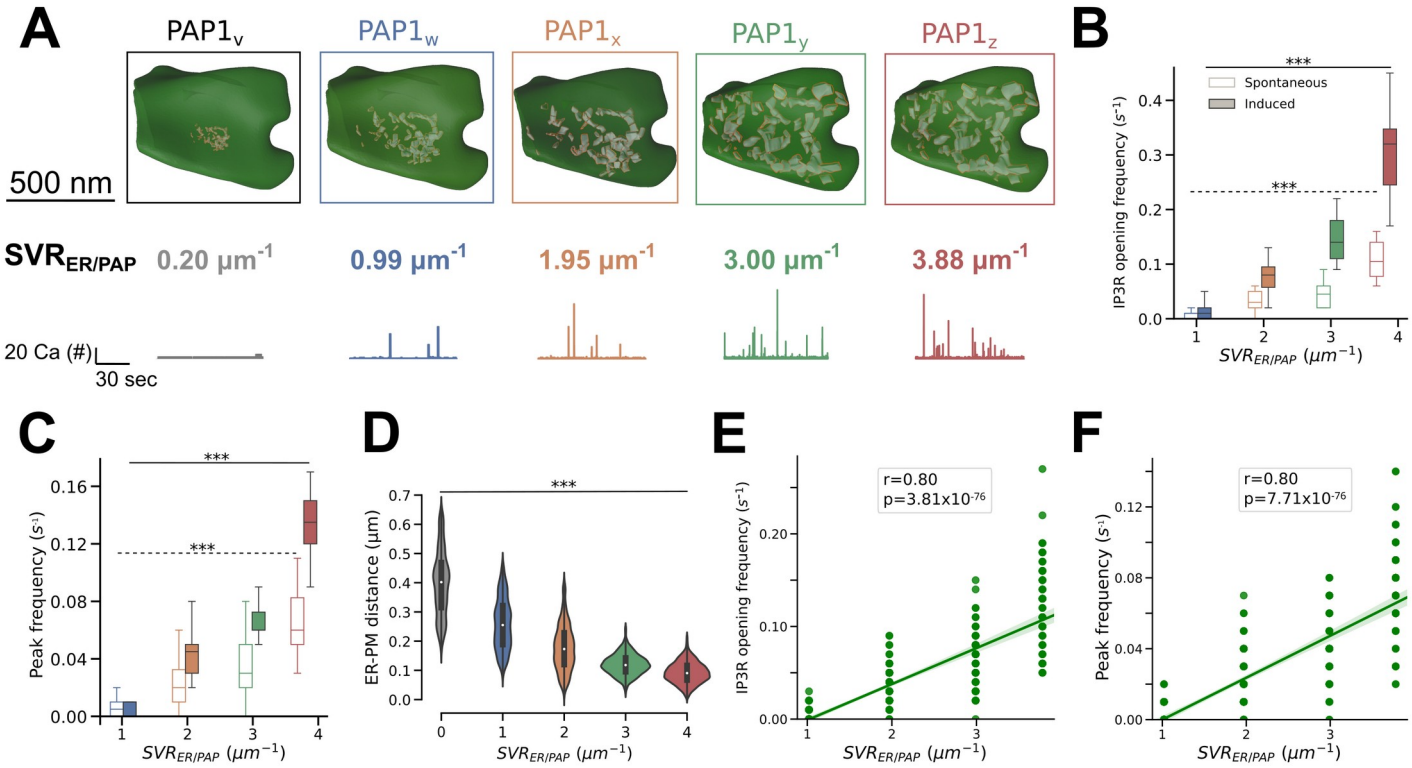
A
PAP1v
PAP1w
PAP1x
PAP1y
PAP1z
500 nm
SVRER/PAP
0.20 µm-1
0.99 µm-1
1.95 µm-1
3.00 µm-1
3.88 µm-1
20 Ca (#)
30 sec
B
Spontaneous
Induced
IP3R opening frequency (s-1)
SVRER/PAP (µm-1)
C
Peak frequency (s-1)
SVRER/PAP (µm-1)
D
ER-PM distance (µm)
SVRER/PAP (µm-1)
E
r=0.80
p=3.81x10-76
IP3R opening frequency (s-1)
SVRER/PAP (µm-1)
F
r=0.80
p=7.71x10-76
Peak frequency (s-1)
SVRER/PAP (µm-1)

Figure 5.

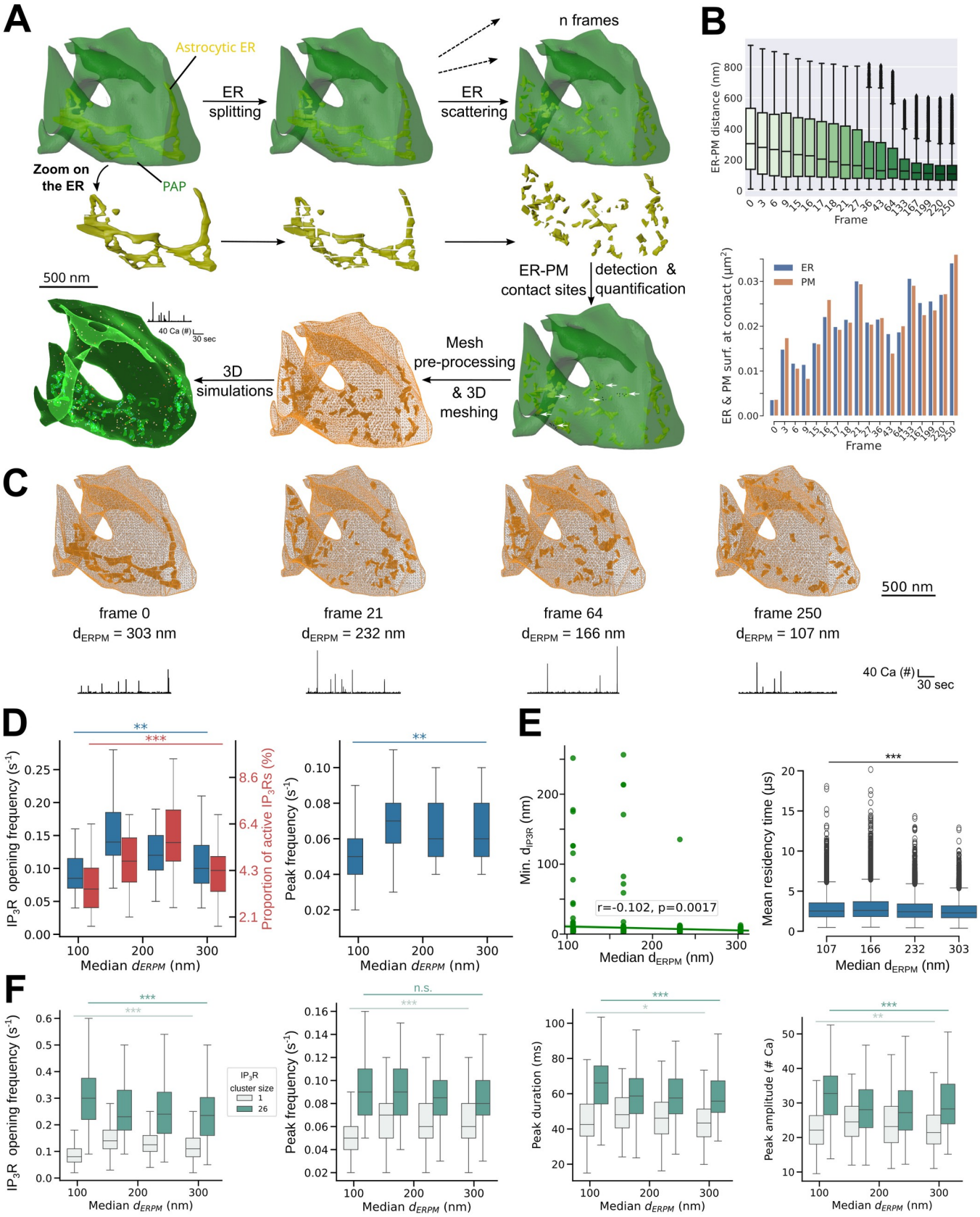
A
Astrocytic ER
ER splitting
ER scattering
n frames
Zoom on the ER
PAP
500 nm
ER-PM contact sites
detection & quantification
Mesh pre-processing & 3D meshing
3D simulations
40 Ca (#)
30 sec
B
ER-PM distance (nm)
Frame
ER
PM
ER & PM surf. at contact (µm²)
C
frame 0
d_ERPM = 303 nm
frame 21
d_ERPM = 232 nm
frame 64
d_ERPM = 166 nm
frame 250
d_ERPM = 107 nm
500 nm
40 Ca (#)
30 sec
D
IP3R opening frequency (s⁻¹)
Proportion of active IP3Rs (%)
Median dERPM (nm)
Peak frequency (s⁻¹)
E
Min. dIP3R (nm)
r=-0.102, p=0.0017
Median dERPM (nm)
Mean residency time (µs)
F
IP3R opening frequency (s⁻¹)
IP3R cluster size
1
26
Peak frequency (s⁻¹)
n.s.
Peak duration (ms)
Peak amplitude (# Ca)
Median dERPM (nm)

Table 1.

Mesh	V_{cyt} (μm^3)	S_{PM} (μm^2)	S_{ER} (μm^2)	$SVR_{ER/PAP}$ (μm^{-1})	d_{ERPM} (nm)	S_{ERc}(μm^2)
$d1s3a107b1$	0.1174	2.00	0.319	2.71	166	4.73×10^{-3}
$d1s8a22b1$	0.3979	8.62	0.0314	0.079	1118	6.27×10^{-4}
$d1s10a24b1$	0.3889	7.68	0.335	0.86	356	1.35×10^{-4}
$d2s6a9b1$	0.5094	10.07	0.238	0.47	455	5.65×10^{-3}
$d9s4a34b1$	0.417	6.92	0.719	1.72	266	7.63×10^{-3}
$d10s1a2b1$	0.552	10.59	0.138	0.25	937	1.41×10^{-3}
$\mathrm{d1s15a32b1_{f0}}$	0.426	6.91	0.85	2.00	303	3.56×10^{-3}
$\mathrm{d1s15a32b1_{f15}}$	0.426	6.91	0.85	2.00	232	1.63×10^{-2}
$\mathrm{d1s15a32b1_{f64}}$	0.426	6.91	0.85	2.00	166	1.87×10^{-2}
$\mathrm{d1s15a32b1_{f250}}$	0.426	6.91	0.85	2.00	107	3.41×10^{-2}
$\mathrm{PAP1_v}$	0.434	3.55	0.088	0.21	402	0
$\mathrm{PAP1_w}$	0.432	3.55	0.428	0.99	255	0
$\mathrm{PAP1_x}$	0.428	3.55	0.834	1.95	173	1.33×10^{-3}
$\mathrm{PAP1_y}$	0.423	3.55	1.27	3.00	118	0
$\mathrm{PAP1_z}$	0.418	3.55	1.62	3.88	91	1.62×10^{-2}

Figure 1: Quantification of the geometrical properties of hippocampal tripartite synapses (A) Diagram presenting the workflow to extract tripartite synapse meshes (illustrated with synapse d10s1a2b1): 1. Synapses in contact with the 220 μm^3 astrocytic volume were selected one by one. 2. A cube of 1.5 μm edge length (3.375 μm^3) was created and centered at the center of mass of the post-synaptic density (PSD, red). 3. Boolean intersection between the neuronal and astrocytic objects and the cube resulted in the isolation of the elements of the tripartite synapse mesh: the perisynaptic astrocytic process (PAP, green), the astrocytic endoplasmic reticulum (ER, yellow), the bouton (grey) and the spine (blue). This workflow resulted in the creation of 44 excitatory and 2 inhibitory tripartite synapse meshes. (B) Boxplots presenting the distribution of the minimum distance between each vertex on the PAP membrane and the center of mass of the PSD, measured in the 27 excitatory tripartite synapse meshes fully reconstructed in this study. (C-F) Boxplots presenting the distribution of spine, bouton, and PAP surface area (C), volume (D), and surface-volume ratio (F). (E) Scatterplot illustrating the increase of Spine volume with Bouton volume. Tripartite synapses in which PAPs contained some ER are represented with blue dots, orange otherwise. (G) Boxplots of median distances between PSD, Bouton, & spine heads to PAPs with (blue, n=20) or without (orange, n=7) ER (top). Distribution of PAP-bouton (left) & PAP-spine (right) distances differentiating PAPs with (blue, n=20) & without (orange, n=7) ER. (H) Scatterplots presenting the variation of median PAP-bouton distance with bouton surface area (left), median PAP-spine distance with spine surface area (middle), and minimum PAP-PSD distance with PAP surface area (right). Scatterplots are presented with a linear regression fit. Spearman

correlation coefficients, r, and p-values, p, are displayed onto each regression plot, n=27.

Figure 2: Characterization of the geometrical properties of the ER in PAPs. (A)

Representative FIB-SEM images highlighting the presence of some endoplasmic reticulum (ER, ref arrowheads) in perisynaptic astrocytic processes (PAPs). (B) Image of the d1s15a32b1 PSD (red) and the neighboring PAP (green), that contains some ER (yellow). (C) Violin plots illustrating the distribution of ER surface area (left), volume (middle) and surface volume ratio (SVR, right) within PAPs, n=20. (D) Among the 27 fully reconstructed PAP meshes extracted, 75 % contained some ER. (E) Distribution of the ratio between the ER surface area and PAP volume (n=20). (F) Distribution of the minimum ER-PSD distance in PAPs, n=20. The lowest ER-PSD distance measured was 70 nm (synapse d4s2a70b1). (G) (Left) Boxplot presenting the distribution of the distance between each ER membrane vertex and the center of mass of the PSD in each PAP, d_{ERPSD}, n=20. (Middle) Scatterplot presenting the negative correlation between the minimum ER-PSD distance and ER surface area. (Right) There is no strong correlation between PAP and ER volume. (H) (Left) Boxplot presenting the distribution of the distance between each PAP plasma membrane (PM) vertex and the closest ER vertex, d_{ERPM}, n=20. Scatterplots presenting the variation of the median d_{ERPM} in PAPs as a function of the minimum d_{ERPSD} (Middle) and bouton surface area (Right). Scatterplots are presented with univariate kernel density estimation curves and a linear regression fit. Spearman correlation coefficients, r, and p-values, p, are displayed onto each regression plot,

n=20.

Figure 3: Reaction-diffusion simulations reveal different spatio-temporal properties of Ca^{2+} signals between PAPs of the same cell. (A) Schematic representation of the model of Ca^{2+} signaling in PAPs used in this study. The model is stochastic, spatially-extended and simulations can be performed in complex 3D meshes. Ca^{2+} influx into the cytosol results from Ca^{2+} channels on the plasma membrane and from IP_3R channels on the ER. At t = 1 s, 50 IP_3 molecules were injected at the plasma membrane of the PAP, simulating neuronal activity. The reactions modeled are detailed in Supplementary Table S2, parameter values and initial conditions in Table S3. (B) Representative Ca-GCaMP traces from simulations in a cylindrical mesh, 200 nm in diameter, 1 *μ*m long (top, black) and experiments (middle, red, [54]). SNR: signal-to-noise ratio (see Methods). (bottom) Ca^{2+} peak amplitude, frequency, and duration of simulated (black) and experimental signals (red) were similar. Data are presented as mean ± standard deviation, n= 20 and 29 for *in silico* and experimental traces, respectively. (C) Images of the 6 PAP meshes in which simulations were performed: d1s3a197b1, d1s8a22b1, d1s10a24b1, d2s6a9b1, d9s4a34b1, and d10s1a2b1 (top) and representative Ca-GCaMP (middle, orange) and free Ca^{2+} (bottom, blue) traces in each mesh. Free Ca^{2+} signals were measured in separate simulations, where no GCaMP was added into the cytosol of the PAP. IP_3R channels and Ca^{2+} channels at the plasma membrane, Ch_{PM}, were randomly distributed onto the ER membrane and plasma membrane, respectively. (D) Quantification of peak frequency of free Ca^{2+} (left, blue, n=20) and Ca-GCaMP (right, orange, n=20) signals measured *in silico* in

3D meshes of the PAPs presented in panel C. (E) Peak frequency (left) and IP_3R opening frequency (right) are positively correlated with the ratio between the ER surface area and the cytosolic volume, $SVR_{ER/PAP}$. (G) Peak frequency (left) and IP_3R opening frequency (right) are negatively correlated with the median distance between each vertex on the PAP plasma membrane and the closest vertex on the ER membrane, d_{ERPM}. Plots are presented with univariate kernel density estimation curves and a linear regression fit. Spearman correlation coefficient, r, and p-value, p, are displayed onto each regression plot.

Figure 4: Ca^{2+} microdomain activity in PAPs increases with ER surface-PAP volume ratio. (A) (Top) Images of the different PAP meshes created to investigate the effect of the ratio between ER surface area and PAP volume, $SVR_{ER/PAP}$, on Ca^{2+} microdomain activity: $PAP1_{v-z}$. Meshes were obtained by rescaling the ER object in PAP1, located at the vicinity of the d9s3a51b1 PSD (Supplementary Fig. S11). Geometrical features of the meshes are presented in Table 1. (Bottom) Representative free Ca^{2+} traces measured in $PAP1_v$ (grey), $PAP1_w$ (blue), $PAP1_x$ (orange), $PAP1_y$ (green) and $PAP1_z$ (red). IP_3R opening frequency (B, ANOVA, $p = 9.70 \times 10^{-83}$ and $p = 7.34 \times 10^{-65}$ for spontaneous and induced Ca^{2+} signals, respectively) and Ca^{2+} peak frequency (C, ANOVA, $p = 3.59 \times 10^{-80}$ and $p = 5.88 \times 10^{-128}$ for spontaneous and induced Ca^{2+} signals, respectively) increase with $SVR_{ER/PAP}$. (D) Quantification of the decrease of ER-PM distance d_{ERPM} with $SVR_{ER/PAP}$ in $PAP1_{v-z}$ meshes. IP_3R opening frequency (E) and peak frequency (F) were positively correlated with

$SVR_{ER/PAP}$. Plots are presented with univariate kernel density estimation curves and a linear regression fit. Spearman correlation coefficient, r, and p-value, p, are displayed onto each regression plot.

Figure 5: The spatial distribution of the ER dictates Ca^{2+} microdomain activity in perisynaptic astrocytic processes. (A) Schematic representing the workflow of the algorithm developed to create synthetic realistic PAP meshes in 3 spatial dimensions with various ER distributions and constant shape, volume and surface area of PAP and ER, used on the PAP mesh d1s15a32b1. The ER is split and a simulation with n frames is generated in Blender, in which ER objects are subject to physical forces that alter their spatial distribution. The n frames are thus characterized by different locations of the ER elements within the PAP, with constant ER and PAP shapes. The pipeline detects, quantifies and exports in a text file the distance between each vertex at the plasma membrane (PM) and the closest vertex at the membrane of the ER. A point cloud can be created to visualize the ER vertices at ER-PM contact sites (ER-PM distance $d_{ERPM} \leq 20$ nm, white arrows). The mesh pre-processing workflow presented in Fig. 3C is then applied to the mesh of each desired frame. The resulting 3D tetrahedral meshes can then be used for 3D reaction-diffusion simulations. (B) (Top) Quantification of the distance between each PM vertex and the closest ER vertex in different frames of the simulation generated by the workflow presented in panel A. (Bottom) Quantification of the ER (blue, left) and PM (orange, right) surface area at ER-PM contact sites, in frames of the simulation generated by the workflow presented in panel A. (C) Images and

representative free Ca^{2+} traces in different meshes created from PAP d1s15a32b1 using the automated workflow presented in panel A: $d1s15a32b1_{fr0}$, $d1s15a32b1_{fr15}$, $d1s15a32b1_{fr64}$, and $d1s15a32b1_{fr250}$, characterized by diverse ER distributions within the PAP with constant PAP and ER shapes, volumes and surface areas. (D) IP_3R opening frequency (left, blue), the proportion of active IP_3Rs (left, red), and Ca^{2+} peak frequency (right) increased with median d_{ERPM} (ANOVA, p = 0.0032, p = 8.19 × 10^{-4}, and p = 0.024, respectively). (E) (left) The minimum distance between two adjacent IP_3R sites decreased with median d_{ERPM}. (right) Mean Ca^{2+} residency time in IP_3R site nanodomains decreases as median d_{ERPM} increases. (F) (left) While in the absence of IP_3R clusters IP_3R opening frequency increased with the median d_{ERPM} (light green, ANOVA, p = 1.62 × 10^{-13}, n=100), it was larger for smaller values of d_{ERPM} when ER-PM contact sites were equipped with IP_3R clusters (dark green, p = 9.9× 10^{-5}). (middle left) Peak frequency increased with d_{ERPM} in the absence of IP_3R clusters (light green, p = 5.87 × 10^{-9}) while no effect was observed upon IP_3R clustering (dark green, p = 0.17). Similarly, Ca^{2+} peak duration (middle right) and amplitude (right) slightly increased with median d_{ERPM} in the absence of clusters (light green, p = 0.014 and p = 5.26 × 10^{-3} for peak duration and amplitude, respectively) while clustering of the Ca^{2+} channels resulted in increased peak duration and amplitude as the median d_{ERPM} decreased (dark green, p = 4.29 × 10^{-4} and p = 1.95 × 10^{-4}, respectively).

Table 1: Characteristics of the 3D PAP meshes used in the reaction-diffusion simulations. V_{cyt} is the cytosolic volume, S_{PM} is the plasma membrane surface area, S_{ER} is the ER surface area, $SVR_{ER/PAP}$ is the ratio

between the ER surface area and the cytosolic volume. d_{ERPM} is the median ER-plasma membrane distance. S_{ERc} is the ER surface area at ER-PM contact sites, i.e. where $d_{ERPM} \leq 20$ nm . d1s15a32b1$_{f0}$, d1s15a32b1$_{f21}$, d1s15a32b1$_{f64}$ and d1s15a32b1$_{f250}$ refer to meshes from frames 0, 21, 64 and 250 of the d1s15a32b1 PAP mesh presented in Fig. 5.